Assessment of localized artificial diffusivity scheme for large-eddy simulation of compressible turbulent flows

Soshi Kawai [a,*], Santhosh K. Shankar [b], Sanjiva K. Lele [b,c]

[a] Center for Turbulence Research, Stanford University, 488 Escondido Mall, Stanford, CA 94305-3035, USA
[b] Department of Aeronautics and Astronautics, Stanford University, 496 Lomita Mall, Stanford, CA 94305-4035, USA
[c] Department of Mechanical Engineering, Stanford University, 496 Lomita Mall, Stanford, CA 94305-4035, USA

ARTICLE INFO

ABSTRACT

The localized artificial diffusivity method is investigated in the context of large-eddy simulation of compressible turbulent flows. The performance of different artificial bulk viscosity models are evaluated through detailed results from the evolution of decaying compressible isotropic turbulence with eddy shocklets and supersonic turbulent boundary layer. Effects of subgrid-scale (SGS) models and implicit time-integration scheme/time-step size are also investigated within the framework of the numerical scheme used. The use of a shock sensor along with artificial bulk viscosity significantly improves the scheme for simulating turbulent flows involving shocks while retaining the shock-capturing capability. The proposed combination of Ducros-type sensor with a negative dilatation sensor removes unnecessary bulk viscosity within expansion and weakly compressible turbulence regions without shocks and allows it to localize near the shocks. It also eliminates the need for a wall-damping function for the bulk viscosity while simulating wall-bounded turbulent flows. For the numerical schemes used, better results are obtained without adding an explicit SGS model than with SGS model at moderate Reynolds number. Inclusion of a SGS model in addition to the low-pass filtering and artificial bulk viscosity results in additional damping of the resolved turbulence. However, investigations at higher Reynolds numbers suggest the need for an explicit SGS model. The flow statistics obtained using the second-order implicit time-integration scheme with three sub-iterations closely agrees with the explicit scheme if the maximum Courant–Friedrichs–Lewy is kept near unity.

© 2009 Elsevier Inc. All rights reserved.

1. Introduction

Significant recent research has focused on the application of direct numerical simulation (DNS) or large-eddy simulation (LES) to compressible turbulent flows that may involve shock waves, contact surfaces, material discontinuities and their interaction with the turbulence. The motivation for compressible DNS or LES is to elucidate the unsteady phenomena such as mixing, combustion, heat-transfer, sound-generation and unsteady load, which may be of interest. A significant challenge in the field of compressible DNS or LES is to establish a numerical scheme that is able to accurately simulate flows involving flow discontinuities, turbulence and their interactions. The numerical algorithm needs to satisfy two competing requirements: the scheme needs to capture different types of discontinuities and also simultaneously resolve the broadband scales of turbulence.

An attractive methodology to capture the discontinuities has been recently proposed by Cook [1] and extended to curvilinear meshes by Kawai and Lele [2] while a high-order compact differencing scheme is used to resolve

---

* Corresponding author. Tel.: +1 650 723 9286.
  E-mail address: skawai@stanford.edu (S. Kawai).

turbulence. Basically these methods are the extension of previous work on hyperviscosity by Cook and Cabot [3,4] and Fiorina and Lele [5]. The main feature of the method is to locally add artificial fluid transport coefficients, such as artificial shear viscosity, bulk viscosity, thermal conductivity and species diffusivity, to physical fluid transport coefficients to capture the discontinuities by smearing the discontinuity over a numerically resolvable scale. The advantages of this method are its simple formulation, low computational cost, ease of implementation, localization of the artificial dissipation terms at the discontinuities (high-resolution characteristics of a high-order compact scheme can be preserved in smooth region), and the lack of a weighting/hybrid algorithm. All these advantages are desirable for compressible DNS or LES of the flows involving shock, contact, and material discontinuities, turbulence and their interactions.

In the context of LES of compressible flows using the localized artificial diffusivity (LAD) method, the recent investigation by Johnsen et al. [6] indicates that the original method is too dissipative for the dilatational motions and damps fluctuations of the thermodynamic properties. This is mainly due to the overly dissipative nature of the original artificial bulk viscosity introduced for shock-capturing. High-derivative (typically fourth-derivative) of strain rate tensor is used as a shock indicator for the original artificial bulk viscosity [4]. Bhagatwala and Lele [7] improved on this drawback by modifying the dimensionless user-specified constant in the strain rate tensor based artificial bulk viscosity model. Mani et al. [8] proposed a simple modification in which the original strain rate tensor based artificial bulk viscosity is replaced by dilatation based bulk viscosity with a negative dilatation switching to improve this drawback. It is more reasonable to use the dilatation θ than the strain rate tensor S for the high-derivative function in the artificial bulk viscosity model since the indicator of S is not able to distinguish shocks from turbulence. However, the question still remains whether the dilatation based high-derivative function used in the model is able to distinguish shocks from expansion and weak compression regions (without shocks) induced by the motions of turbulent eddies on LES grid where the flow is not fully resolved. It is important to localize the artificial bulk viscosity only at shocks not to unnecessarily damp turbulence away from shocks. The artificial bulk viscosity is not required in both expansion and weakly compressible turbulence regions without shocks.

The other unclear issue concerns the relative roles played by the subgrid-scale (SGS) model, low-pass filtering and artificial bulk viscosity. In Ref. [8] the artificial bulk viscosity was coupled with the dynamic Smagorinsky model of Moin et al. [9] with the modification of Lilly [10] in order to account for the subgrid terms. On the other hand, Cook and Cabot [4] showed accurate evolution of the energy spectrum in a high Reynolds number decaying turbulence by using the artificial shear viscosity. In addition to the SGS dissipation terms (according to [4] we loosely regard the artificial shear viscosity as a SGS model throughout the paper) both the numerical approaches [4,8] involve the low-pass filtering scheme and the artificial bulk viscosity which are required to maintain numerical stability. It should be noted that the artificial bulk viscosity also has an impact on the vortical motions [8] although the bulk viscosity mainly affects the dilatational motions. That is, the SGS model, low-pass filtering and artificial bulk viscosity each have some impact on near-grid scale eddies. Their relative roles in determining the wavenumber spectra appears to have been bypassed in the existing literature. The present study explores this question.

The another important aspect for the LAD approach is the coupling with an implicit time-integration scheme. The current artificial diffusivity method is based on adding scalar artificial fluid transport coefficients. This may induce a severe time-step restriction on highly stretched anisotropic meshes due to the viscous Courant–Friedrichs–Lewy (CFL) condition when using explicit time-marching methods. For example, considering a shock that crosses a highly stretched fine mesh region and is not aligned with the mesh, high value of the scalar artificial bulk viscosity is active in the stretched fine mesh region, which may limit the time-step size below the practically acceptable level in explicit time-marching methods. Section 3.4 shows results for such a case where the shocks are within the fine stretched mesh region and the numerical instability was encountered with the explicit method for the maximum inviscid CFL = 0.7. Also, in wall-bounded flow simulations a highly stretched mesh is usually used to resolve the near wall region which impacts the time-step size due to an inviscid CFL limit. In such applications implicit time-marching methods are necessary to reduce the computational time.

The main objective of this paper is to evaluate the performance of the localized artificial diffusivity method on compressible turbulent flows with shocks in the context of LES using compact differencing and low-pass filtering schemes. Emphasis is placed on the improvement of the dilatation based artificial bulk viscosity by employing a switching function (shock sensor), the investigation of the relative roles played by SGS model, low-pass filtering and artificial bulk viscosity, and the effect of the implicit time-integration scheme and the time-step size within the framework of the numerical scheme used in this paper.

In Section 3.1 we first use a model problem to investigate the effect of the dimensionless user-specified constant for the dilatation based bulk viscosity in order to fix the value of the constant that appears in the model. Then, the performance of the switching in the artificial bulk viscosity model, the effect of an explicit SGS model and the impact of the implicit time-integration scheme and the time-step size are addressed through detailed results for the decaying compressible isotropic turbulence with eddy shocklets [11,6] (Section 3.2) and a Mach 3 supersonic turbulent boundary layer (Section 3.3). The numerical results are compared with available DNS data. Finally an illustrative application to the more complex problem of mixing of a choked jet injected into a supersonic crossflow is given in Section 3.4. One-dimensional canonical inviscid shock-related test problems (Sod shock-tube problem [12] and Shu–Osher problem [13]) are provided in Appendix A.

2. Mathematical models

2.1. Governing equations

The compressible Navier–Stokes equations for an ideal non-reactive gas are:

$$\frac{\partial \rho}{\partial t} + \nabla \cdot (\rho \boldsymbol{u}) = 0, \tag{1}$$

$$\frac{\partial \rho \boldsymbol{u}}{\partial t} + \nabla \cdot (\rho \boldsymbol{u}\boldsymbol{u} + p\underline{\boldsymbol{\delta}} - \underline{\boldsymbol{\tau}}) = 0, \tag{2}$$

$$\frac{\partial E}{\partial t} + \nabla \cdot [E\boldsymbol{u} + (p\underline{\boldsymbol{\delta}} - \underline{\boldsymbol{\tau}}) \cdot \boldsymbol{u} - \kappa \nabla T] = 0, \tag{3}$$

$$E = \frac{p}{\gamma - 1} + \frac{1}{2}\rho \boldsymbol{u} \cdot \boldsymbol{u}, \quad p = \rho R T, \tag{4}$$

where ρ is the density, $\boldsymbol{u}$ is the velocity vector, p is the static pressure, E is the total energy, T is the temperature, $\gamma(= 1.4)$ is the ratio of specific heats, R is the gas constant, κ is the thermal conductivity, $\underline{\boldsymbol{\delta}}$ is the unit tensor. The viscous stress tensor $\underline{\boldsymbol{\tau}}$ (for a Newtonian fluid) is

$$\underline{\boldsymbol{\tau}} = \mu(2\underline{\boldsymbol{S}}) + \left(\beta - \frac{2}{3}\mu\right)(\nabla \cdot \boldsymbol{u})\underline{\boldsymbol{\delta}}, \tag{5}$$

where μ is the dynamic (shear) viscosity, β is the bulk viscosity, and $\underline{\boldsymbol{S}}$ is the strain rate tensor, $\underline{\boldsymbol{S}} = \frac{1}{2}(\nabla \boldsymbol{u} + (\nabla \boldsymbol{u})^{\mathsf{T}})$.

In the compressible LES, the Navier–Stokes equations are spatially filtered, that introduce Favre-averaged variables. Spatially filtered Navier–Stokes equations are similar to the Navier–Stokes equations but include additional subgrid-scale stress, heat flux and species diffusion terms that need to be modeled.

2.2. Numerical schemes

The spatially filtered Navier–Stokes equations in conservative form are solved in generalized curvilinear coordinates, where spatial derivatives for convective terms, viscous terms, metrics and Jacobian are evaluated by a sixth-order compact differencing scheme [14]. For any scalar quantity f_i for $1 \leqslant i \leqslant imax$, the finite difference approximation to the first spatial derivative at node i, $\frac{\partial f_i}{\partial \xi_l}$ is obtained by the following formulas:

$$\alpha \frac{\partial f_{i-1}}{\partial \xi_l} + \frac{\partial f_i}{\partial \xi_l} + \alpha \frac{\partial f_{i+1}}{\partial \xi_l} = a\frac{f_{i+1} - f_{i-1}}{2\Delta\xi_l} + b\frac{f_{i+2} - f_{i-2}}{4\Delta\xi_l} \tag{6}$$

where $\alpha = 1/3, a = 14/9$ and $b = 1/9$ for the sixth-order scheme. At boundary points 1 and 2 and correspondingly at $imax$ and $imax-1$, second- and fourth-order one-sided formulas are utilized that retain the tridiagonal form of the equation set [15].

The following eighth($2N$th)-order low-pass spatial filtering scheme [14] is applied to the conservative variables once in each direction after each final Runge–Kutta step or sub-iteration step for the explicit and implicit time-integration schemes in order to ensure numerical stability:

$$\alpha_f \breve{f}_{i-1} + \breve{f}_i + \alpha_f \breve{f}_{i+1} = \sum_{n=0}^{N} \frac{a_n}{2}(f_{i+n} + f_{i-n}), \tag{7}$$

where f_i is the solution vector, and $\breve{f}_i$ is filtered quantity for $1 \leqslant i \leqslant imax$. A eighth-order filter is obtained with $a_0 = \frac{93+70\alpha_f}{128}, a_1 = \frac{7+18\alpha_f}{16}, a_2 = \frac{-7+14\alpha_f}{32}, a_3 = \frac{1-2\alpha_f}{16}, a_4 = \frac{-1+2\alpha_f}{128}$. The α_f is a free parameter satisfying the inequality $-0.5 < \alpha_f \leqslant 0.5$. In this range, as α_f is increased, the filtering is more localized to the high wavenumbers. In the present study, the α_f is fixed to 0.495 unless otherwise noted. High-order one-sided formulas are used for the near boundary points from 1 to 4 and correspondingly from $imax$ to $imax-3$ [16]. Detailed spectral responses of these filters may be found in Ref. [17]. Real part of the modified wavenumber for the first derivative approximation using the sixth-order compact difference scheme and the transfer functions of the eighth-order low-pass filter with $\alpha_f = 0.495, 0.497$ and 0.499 with single, 100 and 1000 times application are given in Fig. 1.

The compact differencing/filtering scheme with the localized artificial diffusivity method is coupled with both explicit and implicit time-integration methods. The classical, four-stage, fourth-order, low-storage form of the Runge–Kutta method (RK4) [18] and the second-order fully implicit scheme (Imp2), called ADI–SGS scheme [19,20], are used for time integration. The ADI–SGS scheme is derived by combining alternative direction implicit (ADI) factorization [21] with the lower-upper symmetric-Gauss–Seidel (LU-SGS) method [22]. Three steps of sub-iterations (Newton–Raphson iteration) are adopted to minimize the errors due to the linearization in the implicit scheme.
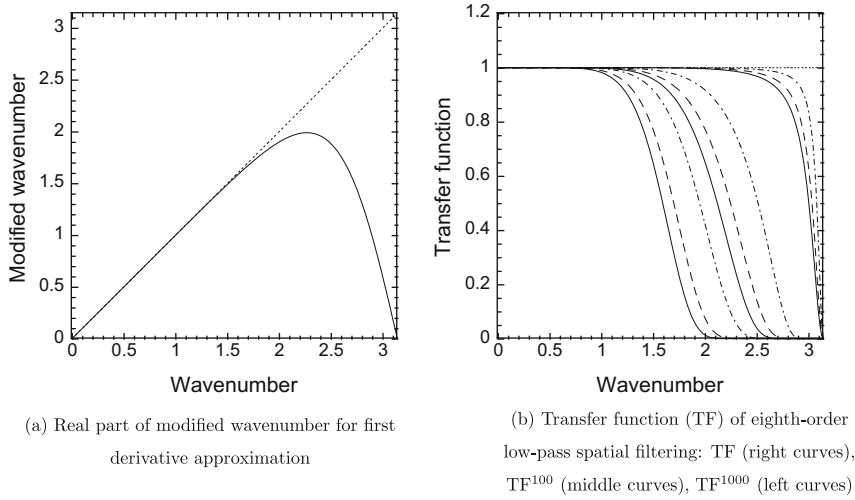
(a) Real part of modified wavenumber for first derivative approximation

(b) Transfer function (TF) of eighth-order low-pass spatial filtering: TF (right curves), TF^{100} (middle curves), TF^{1000} (left curves)

Fig. 1. Characteristics of first spatial derivative approximation and low-pass spatial filtering with single, 100 and 1000 times application. (a): Solid line, sixth-order tridiagonal compact difference scheme; dotted line, exact. (b): Solid line, $\alpha_f = 0.495$; dashed line, $\alpha_f = 0.497$; dashed-dotted line, $\alpha_f = 0.499$; dotted line, no filtering.

2.3. Localized artificial diffusivity (LAD) method

When central differencing schemes, such as high-order compact differencing schemes, are applied to solve flows that involve steep gradients, such as shock waves, contact surfaces or material discontinuities, non-physical spurious oscillations are generated that make the simulation unstable. A key issue here is the identification of an efficient algorithm that ensures the removal of the non-physical spurious oscillations without affecting the physical motions (resolved scales of turbulence).

The discontinuity-capturing scheme used in this study is based on adding grid-dependent artificial fluid transport coefficients to the physical transport coefficients appearing in Eqs. (3) and (5) proposed by Cook [1],

$$\mu = \mu_f + \mu^*, \quad \beta = \beta_f + \beta^*, \quad \kappa = \kappa_f + \kappa^*, \tag{8}$$

where the f subscripts and asterisks denote fluid and artificial transport coefficients, respectively. The artificial fluid transport coefficients are intended to automatically vanish in smooth well-resolved regions of the flow and provide damping in non-smooth unresolved regions to capture different types of discontinuity. Cook [1] designed the artificial coefficients based on a uniformly spaced Cartesian mesh by using high-derivative functions. According to him the artificial fluid properties μ^*, β^* and κ^* serve as a multi-purpose model for the subgrid-scale transport, for shock-capturing and contact surface capturing.

We model the localized artificial diffusivity on a multi-dimensional generalized coordinate system using the curvilinear mesh extension of Kawai and Lele [2] with the length scaling modification of Mani et al. [8]. The localized artificial diffusivity in a general form can be written as:

$$\mu^* = C_\mu \rho \overline{\left| \sum_{l=1}^{3} \frac{\partial^r \mathcal{F}_\mu}{\partial \xi_l^r} \Delta \xi_l^r \Delta_{l,\mu}^2 \right|} \mathcal{D}_\mu^2, \tag{9}$$

$$\beta^* = C_\beta \rho f_{sw} \overline{\left| \sum_{l=1}^{3} \frac{\partial^r \mathcal{F}_\beta}{\partial \xi_l^r} \Delta \xi_l^r \Delta_{l,\beta}^2 \right|} \mathcal{D}_\beta^2, \tag{10}$$

$$\kappa^* = C_\kappa \overline{\frac{\rho c_s}{T} \left| \sum_{l=1}^{3} \frac{\partial^r \mathcal{F}_\kappa}{\partial \xi_l^r} \Delta \xi_l^r \Delta_{l,\kappa} \right|}, \tag{11}$$

where C_μ, C_β and C_κ are dimensionless user-specified constants, $\mathcal{F}_\mu, \mathcal{F}_\beta$ and $\mathcal{F}_\kappa$ are the functions that detect the unresolved subgrid-scale eddies, the steep gradients introduced by shock waves and contact surfaces. The f_{sw} in Eq. (10) is the *switching function (shock sensor)* that is designed to remove unnecessary artificial bulk viscosity in the region without shocks and localize it near shock waves. The $\Delta \xi_l$ and $\Delta_{l,\bullet}$ are the grid spacing in the computational space and physical space. Usually $\Delta \xi_l$ is set to 1. The c_s is sound speed, and ξ_l refers to generalized coordinates ξ, η and ζ when l is 1, 2 and 3, respectively. If r is sufficiently high, the artificial diffusivity is localized in the regions of discontinuity (unresolved high wavenumber k^r content of the flowfield on a given mesh). The overbar denotes an approximate truncated-Gaussian filter [3]. One important aspect for the artificial diffusivity model is to choose the appropriate *detector functions* $\mathcal{F}_\mu, \mathcal{F}_\beta$ and $\mathcal{F}_\kappa$ in Eqs. (9)–(11) to effectively detect different types of discontinuity while automatically deactivating in the regions where subgrid-scale eddies, shock waves and contact surfaces are not present. In this study, $\mathcal{F}_\mu = S$ and $\mathcal{F}_\kappa = e = \frac{1}{\gamma-1} \frac{p}{\rho}$ are chosen as proposed by Cook [1].

For the artificial bulk viscosity, the following four different sets of $\mathcal{F}_\beta$ and f_{sw} are used to evaluate the impact of the artificial bulk viscosity on turbulence in compressible flows with shocks:

1. $\mathcal{F}_\beta = S$ and $f_{sw} = 1$ (essentially the choice of Ref. [4]).
2. $\mathcal{F}_\beta = \nabla \cdot \boldsymbol{u}$ and $f_{sw} = 1$.
3. $\mathcal{F}_\beta = \nabla \cdot \boldsymbol{u}$ and $f_{sw} = H(-\nabla \cdot \boldsymbol{u})$ (the choice of Ref. [8]).
4. $\mathcal{F}_\beta = \nabla \cdot \boldsymbol{u}$ and $f_{sw} = H(-\nabla \cdot \boldsymbol{u}) \times \frac{(\nabla \cdot \boldsymbol{u})^2}{(\nabla \cdot \boldsymbol{u})^2 + |\nabla \times \boldsymbol{u}|^2 + \varepsilon}$.

The proposed improvement (item 4) is to employ the combination of the negative dilatation $H(-\nabla \cdot \boldsymbol{u})$ and the Ducros-type sensor [23] $\frac{(\nabla \cdot \boldsymbol{u})^2}{(\nabla \cdot \boldsymbol{u})^2 + |\nabla \times \boldsymbol{u}|^2 + \varepsilon}$ switching in the dilatation based artificial bulk viscosity model where H is the Heaviside function and $\varepsilon = 10^{-32}$ is the small positive constant to prevent division by zero in the region where both $\nabla \cdot \boldsymbol{u}$ and $\nabla \times \boldsymbol{u}$ are zero. The model enable to localize the artificial bulk viscosity only near shock waves. The negative dilatation switching removes the unnecessary bulk viscosity from expansion regions and the Ducros-type sensor reduces the bulk viscosity at weakly compressible regions without shocks induced by the motions of turbulent eddies. The artificial bulk viscosity is not required in both the expansion and weak compression regions. The $\mathcal{D}_\mu$ and $\mathcal{D}_\beta$ are the wall-damping function for the supersonic wall-bounded viscous flow simulations (Section 3.3) to force the artificial viscosity to vanish in the near wall portion of the boundary layers if necessary. The following Van Driest wall-damping function is used in this paper: $\mathcal{D} = 1 - \exp\frac{-y^+}{A^+}$, where the Van Driest constant A^+ is 26. It was found that κ^* automatically damps in near wall region (also negligibly small throughout the boundary layer). Thus the wall-damping function is not used for the artificial thermal conductivity κ^*. We note that depending on the choice of the detector functions $\mathcal{F}_\mu, \mathcal{F}_\beta$ and $\mathcal{F}_\kappa$ the dimensional scaling constants and the exponent of the length scales $\Delta_{l,\bullet}$ in Eqs. (9)–(11) might need to change in order to retain the proper physical units for μ^*, β^* and κ^*. It should also be noted that the current formulation employs a scalar artificial diffusivity (no directionality) for simplicity thus applying the same value of the artificial diffusion coefficient in every direction.

The $\Delta_{l,\bullet}$ is the grid spacing and is used to scale the artificial diffusivity properly. We define the grid spacing as follows:

$$\Delta_{l,\mu} = |\Delta \boldsymbol{x_l}|, \quad \Delta_{l,\beta} = \left| \Delta \boldsymbol{x_l} \cdot \frac{\nabla \rho}{|\nabla \rho|} \right|, \quad \Delta_{l,\kappa} = \left| \Delta \boldsymbol{x_l} \cdot \frac{\nabla e}{|\nabla e|} \right|. \tag{12}$$

The $\Delta \boldsymbol{x_l}$ is the local displacement vector along the grid line in the ξ_l direction and defined as $\Delta \boldsymbol{x_l} = \left(\frac{x_{i+1} - x_{i-1}}{2}, \frac{y_{i+1} - y_{i-1}}{2}, \frac{z_{i+1} - z_{i-1}}{2} \right)^T$, where the nodes in the ξ_l direction are indexed by i. Thus $\Delta_{l,\beta}$ and $\Delta_{l,\kappa}$ are the grid spacing in the ξ_l direction perpendicular to the shock waves and contact surfaces. The length scaling used here is the natural extension based on Ref. [8] and is an improvement over the scaling defined in Ref. [2].

In the present study $r = 4$ is adopted in Eqs. (9)–(11). Instead of using a series of Laplacians as proposed by Cook and Cabot [4], the fourth derivative $\frac{\partial^4 \mathcal{F}}{\partial \xi_l^4}$ are evaluated by a fourth-order explicit scheme at interior points and second-order schemes near boundary points [2]. This simplification does not lead to tensorial invariance but does not show any major detrimental effect on both the smooth and non-smooth flows (discontinuity-capturing) while significantly reducing computational cost [2].

The dimensionless user-specified constants are set to $C_\mu = 0.002$ and $C_\kappa = 0.01$. The constant C_β is set to 1.0 for the strain rate tensor based artificial bulk viscosity $\mathcal{F}_\beta = S$ and $C_\beta = 1.75$ for the dilatation based bulk viscosity $\mathcal{F}_\beta = \nabla \cdot \boldsymbol{u}$ unless otherwise noted. The different constant for the models gives comparable shock capturing capability in terms of wiggles amplitude and numerical shock thickness (as will be discussed in the following Section 3.1), thus allowing us to make a fair comparison between the models. Fixed values of these constants (as given above) allows the scheme to capture discontinuities for various types of cases. Although the constants work well for wide range of test cases when $r = 4$ in Eqs. (9)–(11) and sixth-order compact/eighth-order filtering schemes are used, the constants might possibly need to be adjusted if different value of r or other numerical schemes are adopted.

3. Numerical results

The study presented here can be broadly classified into three categories: effect of bulk viscosity modeling, SGS modeling and time-integration schemes/time-step size. First we tested a class of artificial bulk viscosity models and SGS models to investigate their performance on compressible turbulent flows. A summary of the numerical methods used in the present study is listed in Table 1 where ASV and DSM are the artificial shear viscosity model and the dynamic Smagorinsky model, respectively. We loosely regard the artificial shear viscosity model as a SGS model throughout the paper. The acronyms for various methods in this table are used in later discussion. The first four cases in the table are used to access the performance of the detector and the switching functions ($\mathcal{F}_\beta$ and f_{sw}) in the artificial bulk viscosity model, while the last three cases aid in judging the effect of SGS modeling. Later in the paper, the effects of the implicit time-integration scheme and the time-step size on compressible turbulent flows within the framework of the numerical scheme developed in this paper are addressed.

Table 1
Summary for localized artificial diffusivity models.

Method	C_β	$\mathcal{F}_\beta$	f_{sw}	SGS model	$\mathcal{D}_\mu$	$\mathcal{D}_\beta$
LAD-S-0	1.0	S	1	None	Inactive	$1 - \exp(-y^+/A^+)$
LAD-D0-0	1.75	$\nabla \cdot \boldsymbol{u}$	1	None	Inactive	$1 - \exp(-y^+/A^+)$
LAD-D1-0	1.75	$\nabla \cdot \boldsymbol{u}$	$H(-\nabla \cdot \boldsymbol{u})$	None	Inactive	$1 - \exp(-y^+/A^+)$
LAD-D2-0	1.75	$\nabla \cdot \boldsymbol{u}$	$H(-\nabla \cdot \boldsymbol{u}) \times \frac{(\nabla \cdot \boldsymbol{u})^2}{(\nabla \cdot \boldsymbol{u})^2 + (\nabla \times \boldsymbol{u})^2 + \varepsilon}$	None	Inactive	1
LAD-D2–ASV	1.75	$\nabla \cdot \boldsymbol{u}$	$H(-\nabla \cdot \boldsymbol{u}) \times \frac{(\nabla \cdot \boldsymbol{u})^2}{(\nabla \cdot \boldsymbol{u})^2 + (\nabla \times \boldsymbol{u})^2 + \varepsilon}$	ASV	$1 - \exp(-y^+/A^+)$	1
LAD-D2–DSM	1.75	$\nabla \cdot \boldsymbol{u}$	$H(-\nabla \cdot \boldsymbol{u}) \times \frac{(\nabla \cdot \boldsymbol{u})^2}{(\nabla \cdot \boldsymbol{u})^2 + (\nabla \times \boldsymbol{u})^2 + \varepsilon}$	DSM	Inactive	1

3.1. Stationary normal shock wave: effect of C_β

Because the dilatation based artificial bulk viscosity model is different from the original strain rate tensor based model, we first investigate the effect of user-specified constants C_β for the dilatation based bulk viscosity. One-dimensional inviscid Mach 2 stationary normal shock wave that corresponds to a pressure jump $p_r/p_l = 4.5$ is used here for the discussions. μ^* and κ^* are turned off ($\mu^* = \kappa^* = 0$) in this test case. Since the LAD-D1 and LAD-D2 reduce to the same scheme for 1D flows, the results of LAD-D1-0 and LAD-D0-0 are shown with C_β ranging between 0 and 2.5. Simulations are performed on a uniformly spaced grid with 101 grid points in the region of $-0.5 \leqslant x \leqslant 0.5 (\Delta x = 0.01)$.

Figs. 2 and 3 show the converged pressure profiles across the stationary shock wave and the maximum wiggles amplitude in a semi-logarithmic plot and numerical shock thickness for C_β ranging between 0 and 2.5 obtained by LAD-D1-0 and LAD-D0-0. In the plot of wiggles amplitude and shock thickness, the original strain rate tensor based bulk viscosity (LAD-S-0) with $C_\beta = 1.0$ is also included. Cook [1] recommended the value of $C_\beta = 1.0$ for the strain rate tensor based bulk viscosity. The wiggles amplitude is normalized by the pressure jump across the shock wave $\Delta p = p_r - p_l$ and the numerical shock thickness is defined by:

$$\frac{\delta}{\Delta x} = \frac{\Delta p}{\Delta x \frac{\partial p}{\partial x}|_{\max}}. \tag{13}$$

There is a clear trade-off between the wiggles amplitude and numerical shock thickness. That is, as C_β increases, the numerical shock discontinuity is smeared and the amplitude of the spurious oscillations decreases. For $C_\beta = 1.75$, the shock is captured over approximately $4\frac{\delta}{\Delta x}$ with the maximum wiggles amplitude of 0.4%. That is comparable to the capability of the shock capturing using Cook's strain rate tensor based bulk viscosity with $C_\beta = 1.0$. LAD-D1-0 and LAD-D0-0 (with and without the negative dilatation switch $H(-\nabla \cdot \boldsymbol{u})$) show almost identical results except the case of $C_\beta = 0.5$. Although one is free to choose the value of C_β, $C_\beta = 1.0$ is used for $\mathcal{F}_\beta = S$ based bulk viscosity model and $C_\beta = 1.75$ is used for $\mathcal{F}_\beta = \nabla \cdot \boldsymbol{u}$ based models for all the test cases discussed in the rest of the paper in order to methodically assess the performance of the detector and switching functions ($\mathcal{F}_\beta$ and f_{sw}) for the artificial bulk viscosity while retaining the comparable shock-capturing capabil-
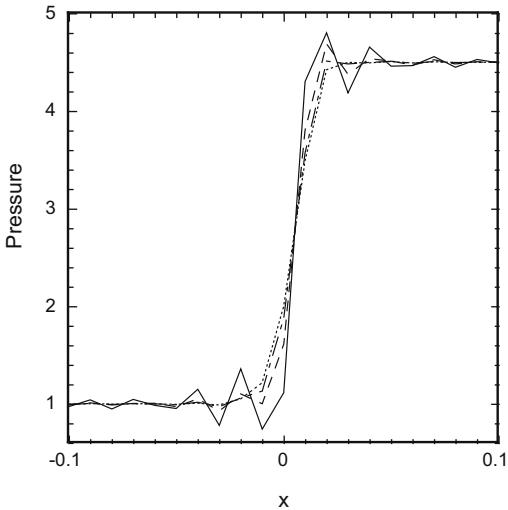

Fig. 2. Pressure profiles across the stationary shock wave with different values of C_β obtained by LAD-D1-0. Solid line, $C_\beta = 0.0$; dashed line, $C_\beta = 0.5$; dashed-dotted line, $C_\beta = 1.0$; dotted line, $C_\beta = 2.0$.
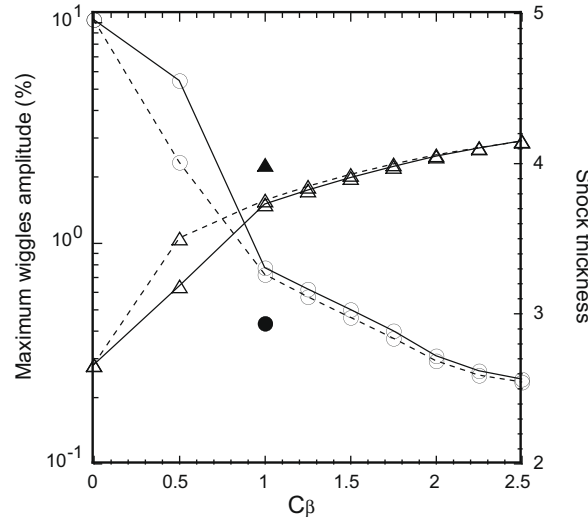
Fig. 3. Maximum wiggles amplitude (%) in a semi-logarithmic scale plotted on left axis with circle and non-dimensionalized numerical shock thickness plotted on right axis with triangle in terms of C_β for the stationary shock wave obtained by LAD-D1-0 and LAD-D0-0. Solid line, LAD-D1-0; dashed line, LAD-D0-0; filled circle and triangle, LAD-S-0 with $C_\beta = 1.0$.

ity. With these value of C_β, $C_\beta = 1.0$ for $\mathcal{F}_\beta = S$ and $C_\beta = 1.75$ for $\mathcal{F}_\beta = \nabla \cdot \boldsymbol{u}$, LAD-D1-0, LAD-D0-0 and LAD-S-0 for the 1D canonical inviscid shock-related test problems (Sod shock-tube problem [12] and Shu–Osher problem [13]) also show almost identical results. The results are given in Appendix A.

3.2. Compressible decaying isotropic turbulence with shocklets

The performance of the various models on the compressible decaying isotropic turbulence with eddy shocklets is investigated here. This 3D test case presents a simple and efficient way for the evaluation of the dissipation characteristics of the numerical models. At a sufficiently high turbulent Mach number, weak shock waves (eddy shocklets) develop spontaneously in the flowfield. The isotropic field can be characterized by the turbulent Mach number and Reynolds number (based on the Taylor micro scale) defined as follows: $M_t = \frac{\sqrt{3}u_{rms}}{\langle c \rangle}$, $Re_\lambda = \frac{\langle \rho \rangle u_{rms}\lambda}{\langle \mu \rangle}$. In the above expressions u_{rms} is given by $u_{rms} = \sqrt{\langle u_i u_i \rangle/3}$. The length scale λ is defined as $\lambda = \frac{1}{3}\sum_i \sqrt{\frac{\langle u_i^2 \rangle}{\left\langle \left(\frac{\partial u_i}{\partial x_i}\right)^2 \right\rangle}}$. The initial field consists of a random solenoidal velocity distribution $u_{i,0}$ which has a power spectra given by, $E(k) \sim k^4 \exp(-2(k/k_0)^2)$. The velocity variance is related to the energy spectra by, $\frac{\langle u_{i,0} u_{i,0} \rangle}{2} = \frac{3u_{rms,0}^2}{2} = \int_0^\infty E(k)dk$. Here the turbulent Mach number in the initial field is chosen to be $M_{t,0} = 0.6$. At this Mach number we see shocklets develop rapidly in the field. The following set of parameters is chosen, $\rho_0 = u_{rms,0} = T_0 = 1, \gamma = 1.4, Pr = 0.7, k_0 = 4, \lambda_0 = 2/k_0 = 0.5, Re_{\lambda,0} = 10^2$. The initial density and pressure fields are set to be constant in the domain, thus indicating that the initial field is not in acoustic equilibrium giving rise to occurrence of strong transient acoustic waves in the field.

The viscosity in the fluid is assumed to obey a power law, $\frac{\mu}{\mu_{ref}} = \left(\frac{T}{T_{ref}}\right)^{0.75}$. The eddy turn over time is used as a time scale as it is defined as $\tau = \lambda_0/u_{rms,0}$. The simulation is run on a 64^3 uniform Cartesian mesh which spans $[0, 2\pi)$ along each axis in the physical domain. A fourth-order Runge–Kutta method with the non-dimensional time step of $\Delta t/\tau = 0.008$ is used for time integration unless otherwise noted. The time step size corresponds to the maximum inviscid CFL number of 0.5. Periodic boundary condition is used in all three directions. The simulations are run till the end time $t/\tau = 4$. The turbulent statistics are averaged over the computational domain and are denoted as $\langle f \rangle$.

The temporal evolution of mean square velocity, variances of density fluctuations and the variances of the vortical and dilatational motions present good metrics for a comparison of the numerical models. Their performance in terms of ability to capture shocklets and at the same time be less dissipative on the statistics of the turbulent flowfield can be judged with this data. The Fourier spectra of velocity, density, dilatation and vorticity yield insight into the range of wave numbers where the artificial diffusivity model is active. The artificial diffusivity models are designed to act mainly in the high wave number range and have minimal influence on the low wavenumber content of the flowfield. Solutions from the DNS on a 256^3 grid are given by Johnsen et al. [6] using the hybrid scheme [24] (sixth-order central differencing in split form + fifth-order finite difference weighted essentially non-oscillatory (WENO) scheme for the interpolation and Roe flux-splitting with entropy fix for the upwinding) and are used as a reference solution in all the comparisons. The reference solutions of spectra are computed using the 256^3 DNS solution at the end time while the reference solution for the temporal evolution of turbulent sta-

tistics is computed from the DNS field that is spectrally filtered from the 256^3 domain to a 64^3 domain. Predictions of the quantities from a seventh-order finite difference WENO [25] on a 64^3 domain are also presented. The data of 256^3 DNS and 64^3 WENO were provided by Dr. J. Larsson and we are grateful for it.

3.2.1. Performance of artificial bulk viscosity

To compare the effect of the detector and switching functions in the artificial bulk viscosity models, simulations of the flowfield are carried out using the methods LAD-S-0, LAD-D0-0, LAD-D1-0 and LAD-D2-0 that are described in Table 1. It should be noted that all models without the low-pass filtering were found to be numerically unstable.

Fig. 4 shows the temporal evolution of various statistics of turbulence. The WENO scheme is seen to under-predict the mean square velocity and variance of vortical motions thus illuminating its dissipative characteristics for broadband motions. When comparing the methods LAD-D2-0, LAD-D1-0 and LAD-D0-0, all of which have the same detector function $\mathcal{F}_\beta$ but differ only in their switching function f_{sw}, the LAD-D2-0 shows superior performance in predicting the density and dilatational variances while the evolutions of the mean square velocity and variance of vorticity exhibit very similar trends in their prediction. The LAD-D2-0 method uses the Ducros-type switch, which reduces the artificial bulk viscosity in proximity of weak compression regions (unlike the LAD-D1-0 method, which has only the negative dilatation switch), is seen to be lesser dissipative on evolution of density and dilatational variances. The variance of pressure and temperature show a similar behavior to that of the density (not shown here). As indicated previously the artificial bulk viscosity is seen to mainly affect dilatational modes but have a certain (minimal) effect on the vortical modes as well. This is seen clearly in Fig. 4(d) where the dilatation based methods, LAD-D2-0, LAD-D1-0 and LAD-D0-0 show very similar evolution for vorticity variance but LAD-S-0 slightly under-predicts the trend. The artificial bulk viscosity based on the strain rate tensor (LAD-S-0) is seen to highly damp the variances of the density and the dilatational motions compared with the dilatation based methods.

This is also evident in the contour plots of dilatation in Fig. 5. The dark spots represents the presence of negative dilatation (eddy shocklets appearing in the flowfield) which is absent when using the LAD-S-0 method which causes excessive damping of dilatation. The LAD-D2-0 scheme preserves the most of the features obtained by the DNS and more closely agrees with the DNS than the LAD-D1-0 and LAD-D0-0. It can be concluded (as in Mani et al. [8]) that dilatation based artificial bulk viscosity model exhibit better capability in predicting the turbulent statistics when compared to the strain rate based artificial bulk viscosity model.
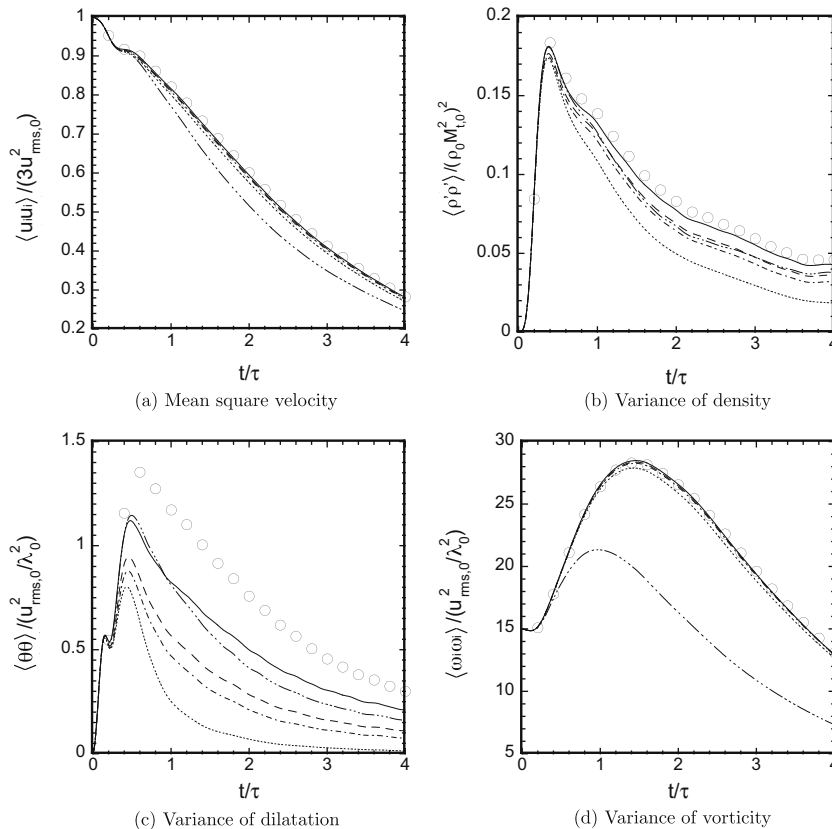

(a) Mean square velocity (b) Variance of density

(c) Variance of dilatation (d) Variance of vorticity

Fig. 4. Comparison of performance of different artificial bulk viscosity models on compressible isotropic turbulence: Temporal evolution of variance of different quantities on a 64^3 grid compared with filtered DNS calculation computed on a 256^3 grid. Circle, filtered DNS; solid line, LAD-D2-0; dashed line, LAD-D1-0; dashed-dotted line, LAD-D0-0; dotted line, LAD-S-0; dashed-triple-dotted line, WENO.
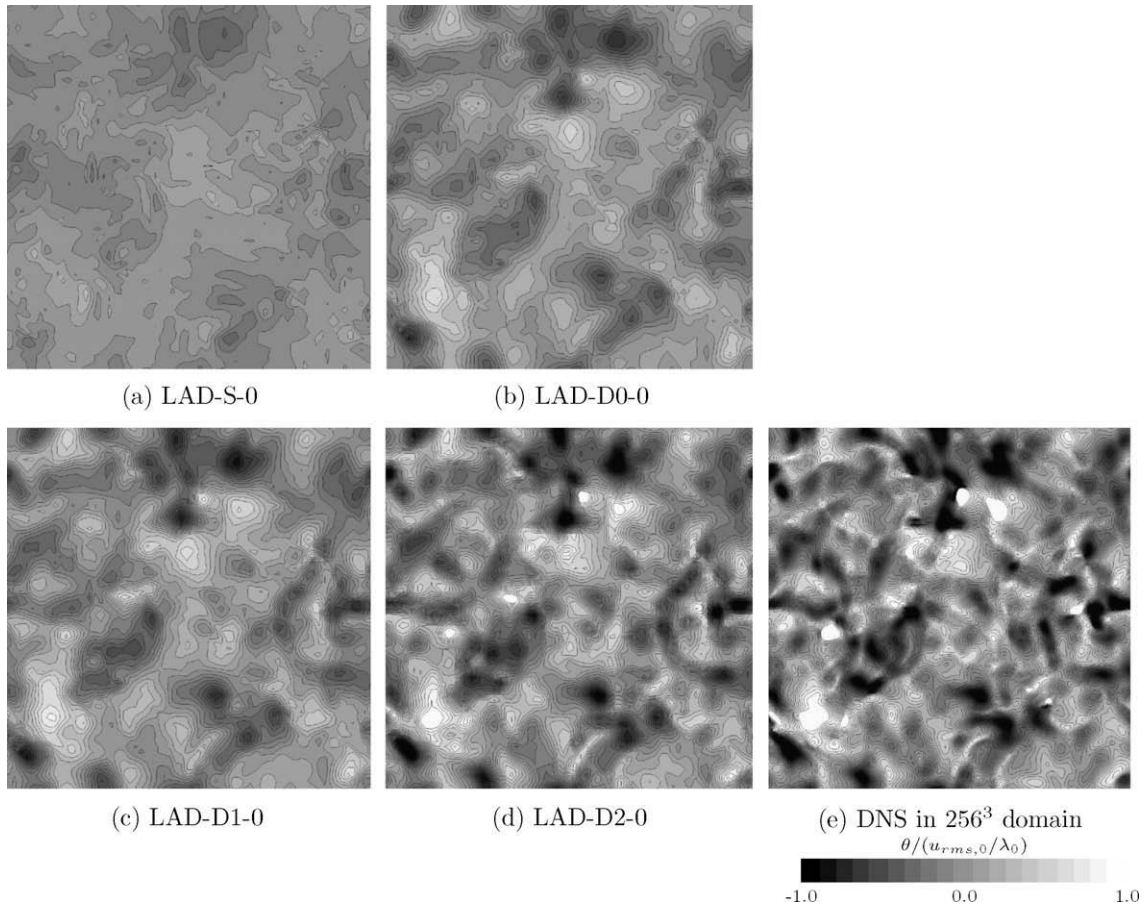
Fig. 5. Contours of dilatation $\theta/(u_{rms,0}/\lambda_0)$ at end time $t/\tau = 4$, 20 equally spaced contours from -1.0 to 1.0. Light and dark colors show positive and negative dilatation.

These observations are further supported when the spectra of velocity, density, dilatation and vorticity are compared in Fig. 6. The LAD-S-0 method is seen to be very dissipative for all density and dilatational modes (low as well as high wave numbers). The WENO scheme shows good agreement with the reference solution for a small range of wavenumbers only. The dilatation based bulk viscosity method with the negative dilatation and the Ducros-type switches (LAD-D2-0) shows good agreement with the reference solution over a large range of wavenumbers. The other dilatation based bulk viscosity methods (LAD-D1-0 and LAD-D0-0) damp the low wavenumber content of density and dilatation spectra.

3.2.2. Role of switching functions in dilatation based artificial bulk viscosity

In this section we clarify the role of the switching function f_{sw} employed in the dilatation based artificial bulk viscosity model. Fig. 7 shows the dilatation and artificial bulk viscosity fields without the application of the approximate truncated-Gaussian filter [the overbar in Eq. (10)] to smoothen the artificial viscosity. The distribution of the sensor components $|\nabla \times \boldsymbol{u}|^2$ and $(\nabla \cdot \boldsymbol{u})^2$ and the sensor functions along the white dashed line in Fig. 7(a) is shown in Fig. 8. The filtered DNS flowfield at $t/\tau = 0.4$ is used for the discussion. The dark spots in Fig. 7(a) represents the presence of shocklets. As expected, the strain rate tensor based model (LAD-S) is activated throughout the domain and unable to distinguish shocks from turbulence (Fig. 7(b)). We also note that the dilatation based model without any switching function (shock sensor) activates at shocks but is also active at expansion and weakly compressible turbulence regions on the LES grid as shown in Fig. 7(c). This leads the damp of the evolution of density and dilatation as discussed in Section 3.2.1. The model without the switching is unable to distinguish shocks from regions of expansion and weakly compressible turbulence regions without shocks. Employing the shock sensor (switching function f_{sw}) in the model shows significant improvements. The negative dilatation switching removes the unnecessary bulk viscosity at expansion regions as shown in Fig. 7(d), which is the choice of Ref. [8]. Differences between the proposed β^* model (LAD-D2) and the model of Ref. [8] (LAD-D1) can be observed in the weakly compressible turbulence regions without shocks as shown in Figs. 7(d) and (e) and 8. The combination of negative dilatation and Ducros-type switching effectively removes the unnecessary artificial bulk viscosity from expansion and weakly compressible turbulence regions and localizes the bulk viscosity near the shocks while the model without the Ducros-type switching is
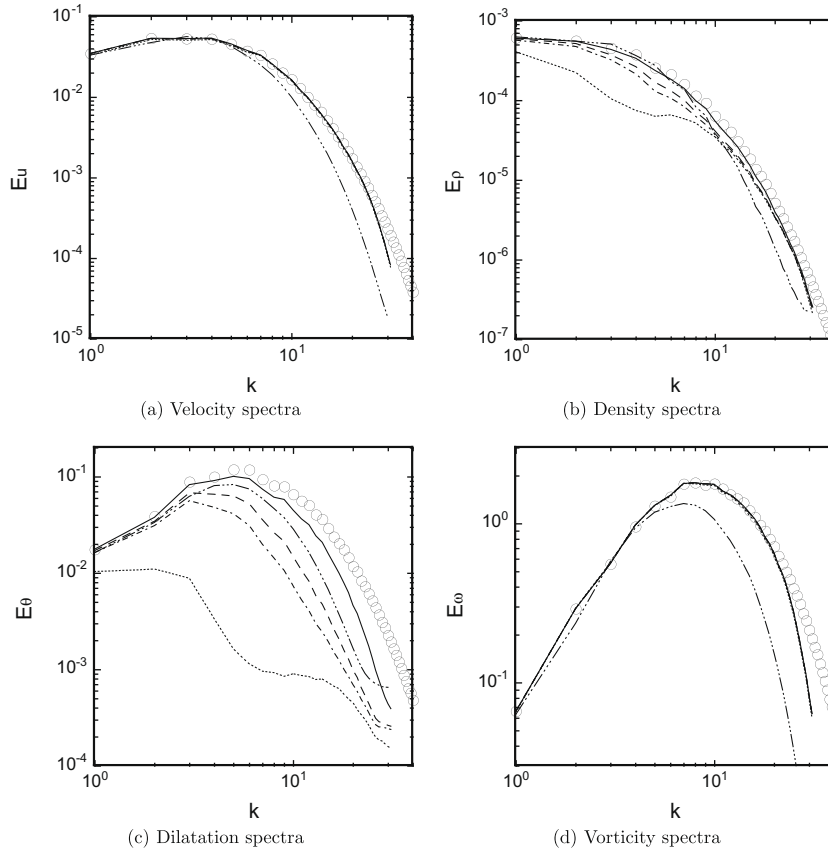
Fig. 6. Comparison of performance of different artificial bulk viscosity models on compressible isotropic turbulence: Spectra at end time $t/\tau = 4$ on a 64^3 grid compared with DNS calculation computed on a 256^3 grid. Circle, DNS on 256^3 grid; solid line, LAD-D2-0; dashed line, LAD-D1-0; dashed-dotted line, LAD-D0-0; dotted line, LAD-S-0; dashed-triple-dotted line, WENO.

unable to distinguish shocks from the weak compression regions without shocks. The proposed β^* is more effective in localizing the artificial viscosity and leads to significant improvements in the compressible isotropic turbulence with shocks while retaining the shock-capturing capability.

The artificial bulk viscosity fields with the application of the approximate truncated-Gaussian filter that are used in the computations are shown in Fig. 9. Without the switching function both the $\mathcal{F}_\beta = S$ and $\nabla \cdot \boldsymbol{u}$ based artificial bulk viscosity (Fig. 9(a) and (b)) are activated throughout the domain while the $\mathcal{F}_\beta = S$ based model gives higher β^* at the turbulence regions. By employing the negative dilatation and Ducros-type switching to localize β^* at shocks, the averaged $\langle \beta^* \rangle$ is reduced by a factor of 9 from that of without switching (Fig. 9(b)) and by a factor of 5 from that of with negative dilatation switching (Fig. 9(c)).

In this section the need for a shock sensor (switching function) in combination with artificial bulk viscosity was emphasized. The shock sensor used in this study (the combination of the Ducros-type sensor and the negative dilatation sensor) significantly improves the performance of artificial bulk viscosity. We note that the present shock sensor may not be the only choice. The choice of an effective shock sensor suitable for a broad range of shock–turbulence problems remains an open question. To avoid introducing additional empirical coefficients we use the combination of the Ducros-type sensor and the negative dilatation sensor. The hypothesis of weakly compressible turbulence assumed in the Ducros-type switching is supported by the low level of dilatation compared to enstrophy within the shock-free turbulent flow as shown in Fig. 8(a). Note that the Ducros-type sensor has been successfully applied to variety of LES and DNS of compressible turbulent flows to identify shocks [23,24,26–31]. However, if the hypothesis of weakly compressible turbulence is not valid then a different sensor may be required.

3.2.3. Effect of SGS models

Using the LAD-D2 model for the artificial bulk viscosity the performance of the artificial shear viscosity model (loosely regarded as a SGS model) and the dynamic Smagorinsky model [9,10] on the isotropic turbulence problem is evaluated. First the results obtained for the fixed values of $Re_{\lambda,0} = 10^2$ and $\alpha_f = 0.495$ are shown. In Figs. 10 and 11 the LAD-D2-0 method (no explicit SGS model), LAD-D2–ASV (artificial shear viscosity model) and the LAD-D2–DSM (dynamic Smagorinsky model) are
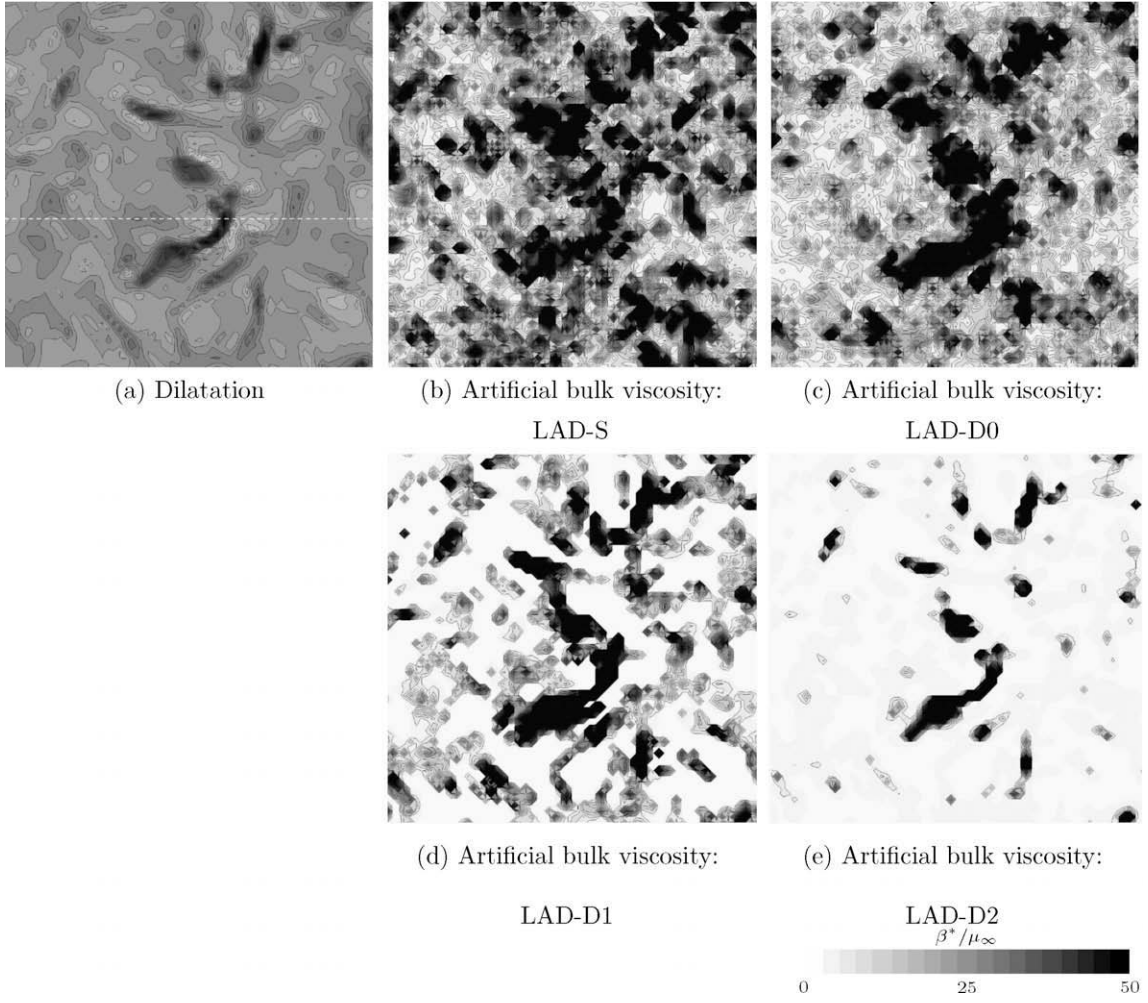
(a) Dilatation

(b) Artificial bulk viscosity: LAD-S

(c) Artificial bulk viscosity: LAD-D0

(d) Artificial bulk viscosity: LAD-D1

(e) Artificial bulk viscosity: LAD-D2

Fig. 7. Role of switching function f_{sw} on dilatation based artificial bulk viscosity. Contours of dilatation $\theta/(u_{rms,0}/\lambda_0)$ and artificial bulk viscosity β^*/μ_∞ without applying the approximate truncated-Gaussian filter at $t/\tau = 0.4$ based on the filtered DNS flowfield. Twenty equally spaced contours from -7.0 to 7.0 for dilatation and from 0.0 to 50.0 for artificial bulk viscosity.

(a) Sensor components
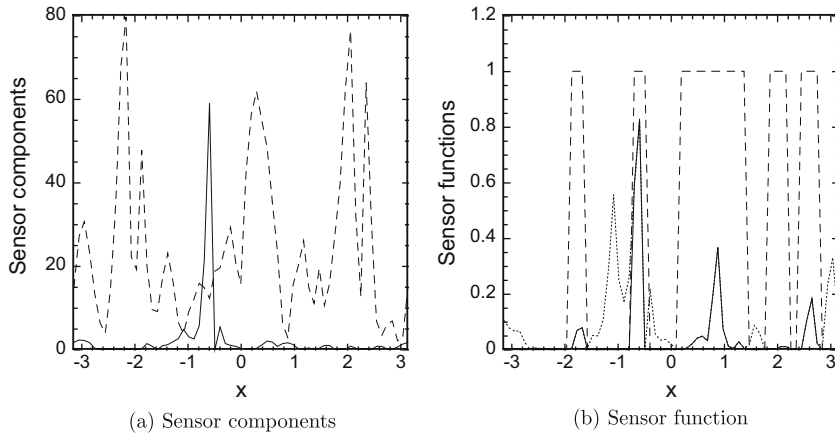
(b) Sensor function

Fig. 8. Distribution of sensor components and switching functions. (a): Solid line, $(\nabla \cdot \boldsymbol{u})^2$; dashed line, $|\nabla \times \boldsymbol{u}|^2$. (b): Solid line, negative dilatation with Ducros switch $f_{sw} = H(-\nabla \cdot \boldsymbol{u}) \times \frac{(\nabla \cdot \boldsymbol{u})^2}{(\nabla \cdot \boldsymbol{u})^2 + |\nabla \times \boldsymbol{u}|^2 + \varepsilon}$; dashed line, negative dilatation switch $f_{sw} = H(-\nabla \cdot \boldsymbol{u})$; dotted line, Ducros switch $f_{sw} = \frac{(\nabla \cdot \boldsymbol{u})^2}{(\nabla \cdot \boldsymbol{u})^2 + |\nabla \times \boldsymbol{u}|^2 + \varepsilon}$.

(a) LAD-S: $\langle \beta^*/\mu_\infty \rangle = 22.6$ (b) LAD-D0: $\langle \beta^*/\mu_\infty \rangle = 19.0$

(c) LAD-D1: $\langle \beta^*/\mu_\infty \rangle = 10.1$ (d) LAD-D2: $\langle \beta^*/\mu_\infty \rangle = 2.1$

β^*/μ_∞
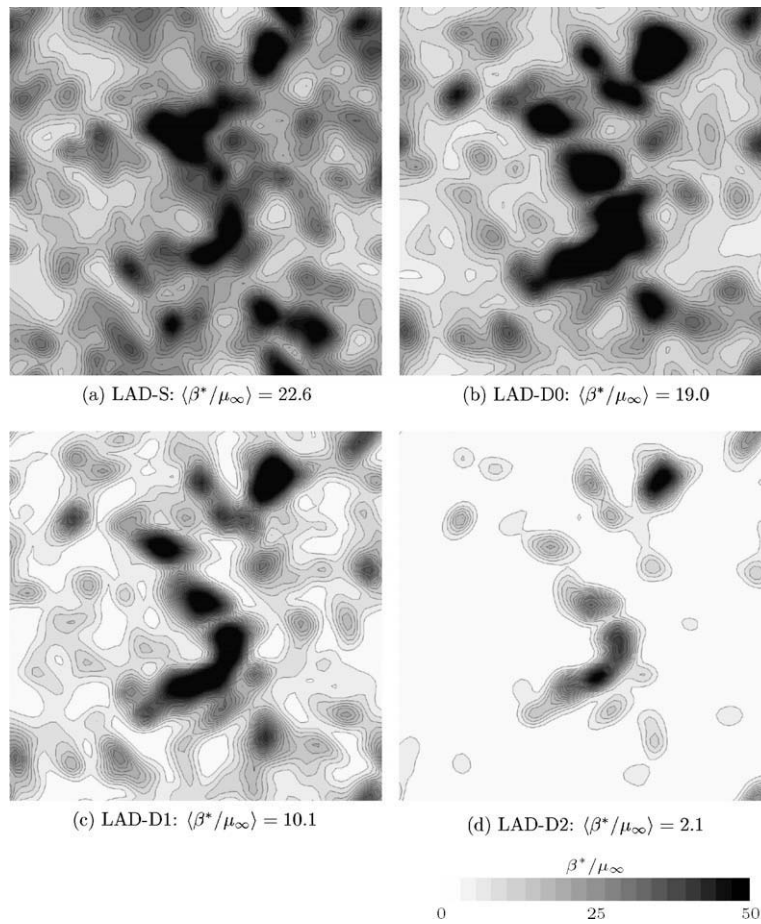
0   25   50

Fig. 9. Contours of artificial bulk viscosity β^*/μ_∞ and averaged bulk viscosity $\langle \beta^*/\mu_\infty \rangle$ at $t/\tau = 0.4$ based on the filtered DNS flowfield. Twenty equally spaced contours from 0.0 to 50.0.

(a) Mean square velocity   (b) Variance of vorticity
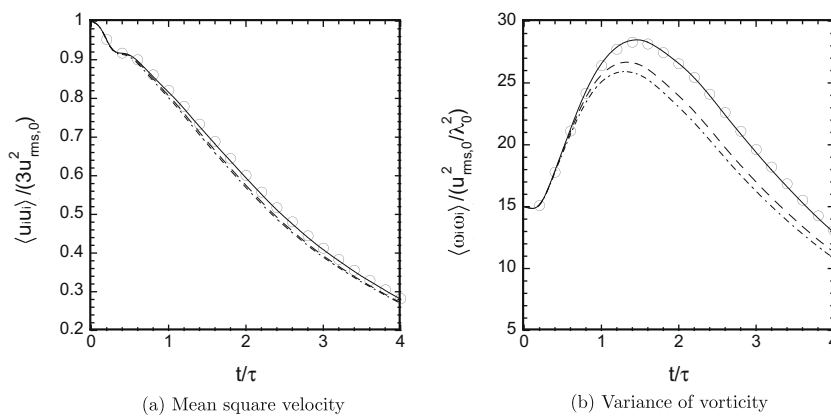
Fig. 10. Comparison of the effect of SGS models on compressible isotropic turbulence: Temporal evolution of variance of velocity and vorticity in comparison with filtered DNS calculation computed on a 256^3 grid. Circle, filtered DNS; solid line, LAD-D2-0; dashed line, LAD-D2–ASV; dashed-dotted line, LAD-D2–DSM.

compared with the reference DNS solution in terms of the temporal evolution and spectra of velocity and vorticity. A common trend is noticed in these figures. Under the conditions examined, adding an explicit SGS model is seen to result in additional damping of the resolved turbulence and somewhat under-predicts the turbulence field statistics. The artificial shear
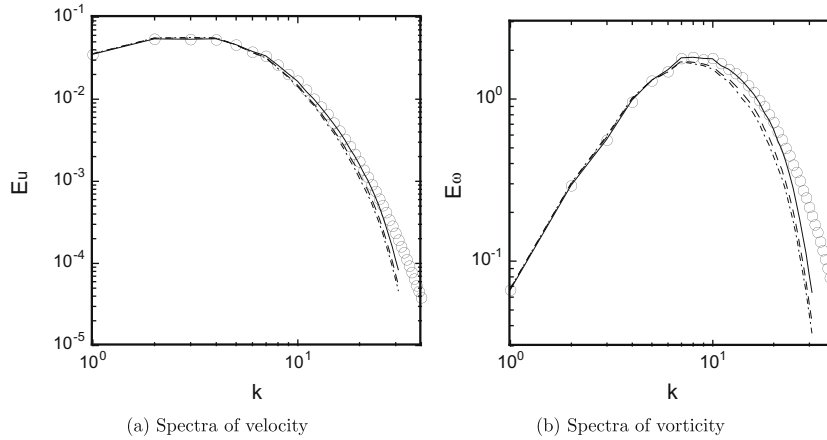
(a) Spectra of velocity   (b) Spectra of vorticity

Fig. 11. Comparison of the effect of SGS models on compressible isotropic turbulence: Spectra of velocity and vorticity at end time $t/\tau = 4$ in comparison with DNS calculation computed on a 256^3 grid. Circle, DNS on 256^3 grid; solid line, LAD-D2-0; dashed line, LAD-D2–ASV; dashed-dotted line, LAD-D2–DSM.

viscosity model shows slightly less damping than the dynamic Smagorinsky model. The variance and spectra of density and dilatation also show a similar behavior (not shown here).

As mentioned before in the discussion of numerical schemes, the solver is coupled with an eighth-order high wavenumber filter applied to the conservative variables in each direction after each final Runge–Kutta step. The cut-off property of the filter is suspected to have a significant influence on the evolution of the flow variables and the derived quantities. In order to investigate the effect of the SGS models further it is necessary to explore their behavior for different filter coefficients α_f (higher α_f is a more high-wavenumber biased filter) and for different Taylor scale Reynolds number. The Taylor scale Reynolds numbers are increased in factors of 10 from the present case where $Re_\lambda = 10^2$. The performance of the three schemes, LAD-D2-0, LAD-D2–ASV and LAD-D2–DSM, are studied in a two-dimensional parameter space of $\alpha_f = 0.495, 0.497$ and 0.499 and $Re_\lambda = 10^2, 10^3, 10^4$ and 10^5. Detailed investigation of the temporal evolution and spectral content of the turbulent flowfield is carried out for all the combinations. Figs. 12 and 13 present some highlights of this study.

Fig. 12 shows the temporal evolution of mean square velocity and vorticity variance for three different Reynolds numbers for the three different SGS models. The results with the filter coefficient $\alpha_f = 0.495$ are shown on the left and the results with $\alpha_f = 0.497$ are on the right. As the Reynolds number is increased, the evolution for each different model progressively becomes insensitive to the Reynolds number and tend to converge. The evolutions at $Re_\lambda = 10^4$ and 10^5 are almost identical (not shown). The results suggest that the low-pass filtering, artificial bulk viscosity and SGS models (when used for LAD-D2–ASV and LAD-D2–DSM) affect the flowfield for the high Reynolds number cases. By comparing Fig. 12(a) and (b) the energy containing fluctuations (the variances of the velocity and thermodynamic properties) are insensitive to the filter coefficient (we only show the velocity variance here) although the vorticity variance (and dilatation variance although not shown) is filter dependent at the high Reynolds numbers. The predicted velocity and vorticity variance (and density and dilatation fluctuations although not shown here) show large sensitivity to the SGS model with increasing the Reynolds number. The methods with an explicit SGS model (LAD-D2–ASV and LAD-D2–DSM) limit the growth of vorticity variance and do not encounter the numerical instability at the high Re_λ for $\alpha_f = 0.495$ and 0.497. Higher peak values are reached as Re_λ is increased but the peak values reached for 10^5 are close to those for 10^4 (not shown). Numerical instability was encountered with the LAD-D2-0 method for $\alpha_f = 0.495$ at $Re_\lambda = 10^4$ and 10^5 and $\alpha_f = 0.497$ at $Re_\lambda = 10^3, 10^4$ and 10^5. Note that some curves in Fig. 12 stop at a finite time due to the numerical instability. All methods explored in this paper regardless of the inclusion of the explicit SGS model encounter numerical instability for $\alpha_f = 0.499$ with $Re_\lambda = 10^3, 10^4$ and 10^5 (not shown here). These results illustrate the relative roles played by the explicit SGS model, low-pass filtering and artificial bulk viscosity and suggest the need for including an explicit SGS model for the higher Reynolds numbers (highly under-resolved cases).

This is further supported when wavenumber spectra are compared. Fig. 13 shows the vorticity spectra at $t/\tau = 2.6$ for the three different Reynolds numbers with $\alpha_f = 0.495$. The evolution of vorticity variance obtained by the LAD-D2-0 for $Re_\lambda = 10^3$ and 10^5 shows a peak close to this time. It is clearly seen that for the high Re_λ, the inclusion of an explicit SGS model is necessary to remove the high energy at the unresolved high wavenumbers.

The results summarized here illustrate the relative roles played by the physical viscosity, low-pass filtering, the SGS models and artificial bulk viscosity. It is reasonable to conclude that for the moderate Reynolds number and turbulent Mach numbers, the inclusion of the explicit SGS model results in additional damping of the resolved turbulence and under-predicts the turbulence field statistics. In addition to the effect of physical viscosity, artificial bulk viscosity and the low-pass filter (applied to the conservative variables after each time-step) provide enough numerical damping to handle physical discontinuities, unresolved scales and the non-physical spurious oscillations from the discretization scheme. However, the results of the high Reynolds numbers (highly under-resolved cases) suggest the need for inclusion of a SGS model. Simulations without
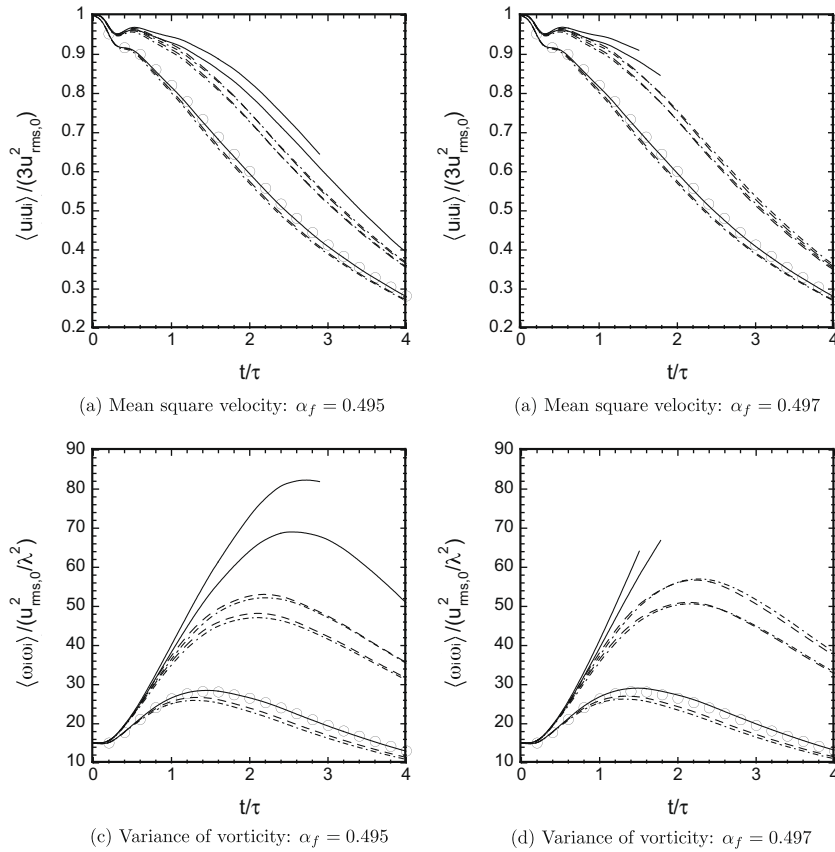
(a) Mean square velocity: $\alpha_f = 0.495$

(a) Mean square velocity: $\alpha_f = 0.497$

(c) Variance of vorticity: $\alpha_f = 0.495$

(d) Variance of vorticity: $\alpha_f = 0.497$

Fig. 12. Comparison of the effect of SGS models for different Reynolds numbers: Temporal evolution of mean square velocity and variance of vorticity with filter coefficient $\alpha_f = 0.495$ and 0.497. $Re_\lambda = 10^2$ (lower curves), $Re_\lambda = 10^3$ (middle curves) and 10^5 (upper curves). Solid line, LAD-D2-0; dashed line, LAD-D2–ASV; dashed-dotted line, LAD-D2–DSM.
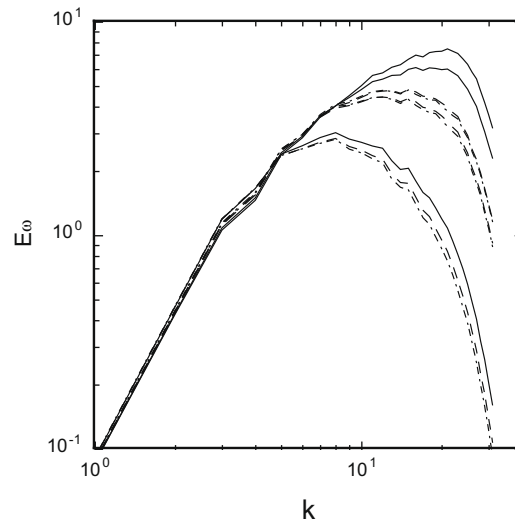
Fig. 13. Comparison of the effect of SGS models for different Reynolds numbers with $\alpha_f = 0.495$: Vorticity spectra at $t/\tau = 2.6$. $Re_\lambda = 10^2$ (lower curves), $Re_\lambda = 10^3$ (middle curves) and 10^5 (upper curves). Solid line, LAD-D2-0; dashed line, LAD-D2–ASV; dashed-dotted line, LAD-D2–DSM.

the SGS model encounter numerical instability at high $Re_\lambda (\geqslant 10^4)$ when using $\alpha_f = 0.495$ and $Re_\lambda \geqslant 10^3$ using $\alpha_f = 0.497$. The introduction of SGS model prevents the instability.

3.2.4. Effect of implicit time-integration scheme and time-step size

For the isotropic turbulence problem the need of implicit time-marching does not arise, because of the absence of regions of highly stretched mesh. Nonetheless the accuracy of the implicit time-integration is investigated by varying the time-step size. Simulations are performed by the second-order fully implicit scheme (Imp2) with the time-step size $\Delta t/\tau$ of 0.008, 0.016, 0.032 and 0.05. The corresponding maximum inviscid CFL numbers are 0.5, 1.0, 2.0 and 3.2. The LAD-D2-0 method is used for the artificial bulk viscosity. Three sub-iterations are carried out within each implicit time-step.

Fig. 14 shows the temporal evolution of the statistics of turbulence with varying the time-step size in the implicit time-marching method. The results of the explicit time-integration scheme (RK4) with $\Delta t/\tau = 0.008$ are also included for comparisons. With the two smallest time-steps size $\Delta t/\tau = 0.008$ and 0.016, the implicit time-integration method predicts the mean square velocity, the density and dilatational variances which are in very good agreements with the explicit time-integration method while the slight differences are observed in the predicted vorticity variance. The variance of vorticity shows the slight increase in the evolution by increasing the time-step size. In the present test we fix the number of low-pass filtering application per time-step. The low-pass filtering scheme is applied once in each direction after each final sub-iteration step, which indicates the less filtering per eddy turn over time by increasing the time-step size. Although not shown here, the results obtained with $\Delta t/\tau = 0.008$ with filtering once per time-step and $\Delta t/\tau = 0.016$ with filtering twice per time-step are almost identical. Thus we conclude that the slight increase in the evolution of the variance of vorticity by increasing the time-step size from $\Delta t/\tau = 0.008$ to 0.016 is due to the less low-pass filtering per eddy turn over time. The results illustrate the filter sensitivity to the predicted vorticity variance while the other turbulent statistics are insensitive to the filtering. The results with the large computational time-steps of $\Delta t/\tau = 0.032$ and 0.05, corresponding maximum CFL numbers of 2.0 and 3.2, show the delay in the evolution and damping of the turbulence, noticeably seen in the density and dilatational variances.

3.3. Supersonic turbulent boundary layer

The next test case is a Mach 3 adiabatic flat plate turbulent boundary layer at Reynolds number of $Re_\delta = 2.0 \times 10^4$ where δ is the boundary layer thickness at the inlet. This problem can be used to assess the capability of the localized artificial diffusivity approach on the wall-bounded compressible turbulent flow.
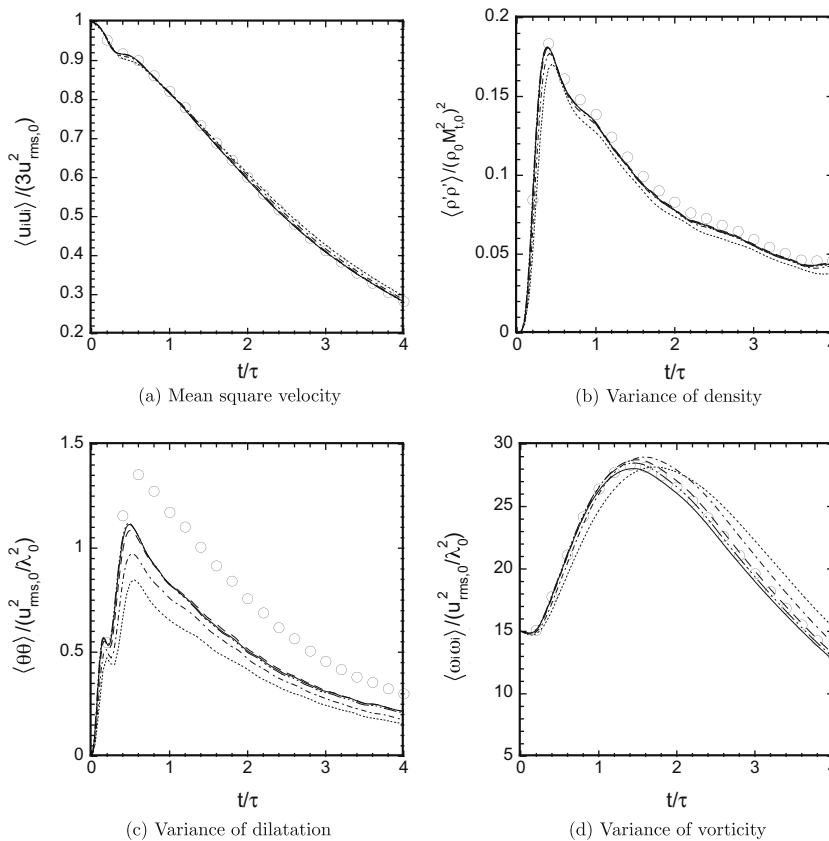

(a) Mean square velocity

(b) Variance of density

(c) Variance of dilatation

(d) Variance of vorticity

Fig. 14. Comparison of the effect of implicit time-integration scheme and time-step size on compressible isotropic turbulence: Temporal evolution of variance of different quantities on a 64^3 grid compared with filtered DNS calculation computed on a 256^3 grid Circle, filtered DNS; solid line, Imp2 $\Delta t/\tau = 0.008$; dashed line, Imp2 $\Delta t/\tau = 0.016$; dashed-dotted line, Imp2 $\Delta t/\tau = 0.032$; dotted line, Imp2 $\Delta t/\tau = 0.05$; dashed-triple-dotted line, RK4 $\Delta t/\tau = 0.008$.

Since the LES of a supersonic turbulent boundary layer involves a wall-bounded viscous flow simulation, the Van Driest wall-damping function in the localized artificial diffusivity scheme is required for the LAD-S, LAD-D0 and LAD-D1 models to force the artificial bulk viscosity to vanish in the near wall portion of the boundary layers. Without the wall-damping function, the methods introduce high artificial bulk viscosity near the wall, which limits the time-step size to be extremely small due to the viscous CFL condition. Note that the LAD-D2 method does not require the wall-damping function, which automatically damps the unnecessary artificial bulk viscosity within the boundary layer and removes the unnecessary time-step restriction. The Ducros-type sensor removes the bulk viscosity in weak compression regions within the boundary layer.

A compressible extension of the rescaling-reintroducing method [32] is used to generate the inflow conditions for the LES. Fig. 15 shows a schematic of this simulation. Instantaneous streamwise velocity contours at the inlet and wall-parallel plane close to the wall ($y^+ = 20.7$) obtained by LAD-D2-0 are shown. The flow quantities at the 12δ downstream location are rescaled and reintroduced for the inflow conditions. Typical low-speed streaks (dark colored regions) are clearly observed. The domain size for the LES is 15δ, 5δ and 15δ in streamwise, spanwise and wall-normal directions. A uniform grid spacing, $\Delta x^+ = 20$ and $\Delta z^+ = 10$, is used in streamwise and spanwise directions. In the wall-normal direction, the grid is clustered near the wall region from $y/\delta = 0$ to 1 and then a uniformly spaced grid is used for $y/\delta = 1$ to 2.5δ. The maximum grid stretching factor in the normal direction is 1.15 and the grid resolutions at the wall and uniformly spaced region are $\Delta y^+_{wall} = 1$ and $\Delta y^+_{unif} = 20$. Sponge layer with the length of 12.5δ is placed at the upper boundaries to remove turbulent fluctuations and their reflection from the boundary.

The second-order implicit time-integration scheme (Imp2) with a non-dimensional time-step of $\Delta t c_{s,\infty}/\delta = 0.0025$ and three sub-iterations is used for the time integration unless otherwise noted. This time-step size corresponds to a maximum inviscid CFL number of 0.88 and $\Delta t^+ = \Delta t u^2_\tau/\nu = 0.1$ in wall units. Based on the incompressible turbulent channel flow computations by Choi and Moin [33], the time-step size should maintain the error from the implicit time-marching scheme to be sufficiently small. In the following, the statistics are averaged in time and in the spanwise direction and are denoted as $\langle f \rangle$. The results are obtained at the location of $x = 12\delta$.

3.3.1. Performance of artificial bulk viscosity

The performance of the detector $\mathcal{F}_\beta$ and switching functions f_{sw} in the artificial bulk viscosity model is addressed by comparing the LAD-S-0, LAD-D0-0, LAD-D1-0 and LAD-D2-0. The mean streamwise velocity profile in a semi-logarithmic plot using Van Driest transformation [34], $U^+_{VD} = \int_0^{U^+} \left(\frac{\rho}{\rho_w}\right)^{1/2} dU^+$, the variances of three velocity components, thermodynamical variables and dilatation are plotted in Fig. 16. The variances of three velocity components obtained by the DNS of Mach 2 supersonic turbulent boundary at $Re_\delta = 1.74 \times 10^4$ by Pirozzoli et al. [35] are also included in Fig. 16(b) for comparisons although the flow conditions are not matched. The variances of temperature, density and pressure are non-dimensionalized by their freestream values. In the mean streamwise velocity profiles, all cases are in good agreement with a fully developed turbulent boundary layer profile with a logarithmic region appearing clearly in the range of $30 < y^+ < 150$. The variance of the dilatation shows the most distinct difference between the four different models. Similarly to the compressible isotropic turbulence, the LAD-S-0 damps the dilatational motions throughout the boundary layer. The LAD-D2-0 shows slightly higher dilatation variance than the LAD-D1-0 and LAD-D0-0, which suggests that the Ducros-type switching reduces the bulk viscosity at weak compression regions within the boundary layer. For the other fluctuation quantities, the dilatation based artificial bulk viscosity (LAD-D0-0, LAD-D1-0 and LAD-D2-0) are almost identical. The results show reasonable agreement with the available DNS data in the velocity fluctuations. Slightly less fluctuations in pressure is observed by the LAD-S-0 compared
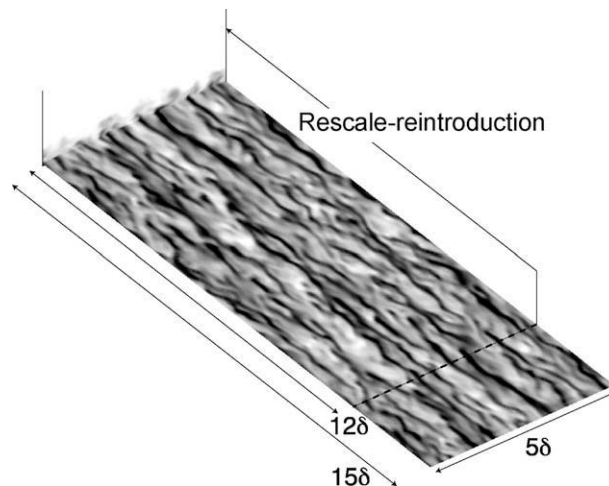

Fig. 15. Schematic of the LES of supersonic turbulent boundary layer. Instantaneous streamwise velocity contours at the inlet and wall-parallel plane close to the wall ($y^+ = 20.7$) obtained by LAD-D2-0. Light and dark colors show high and low streamwise velocity.
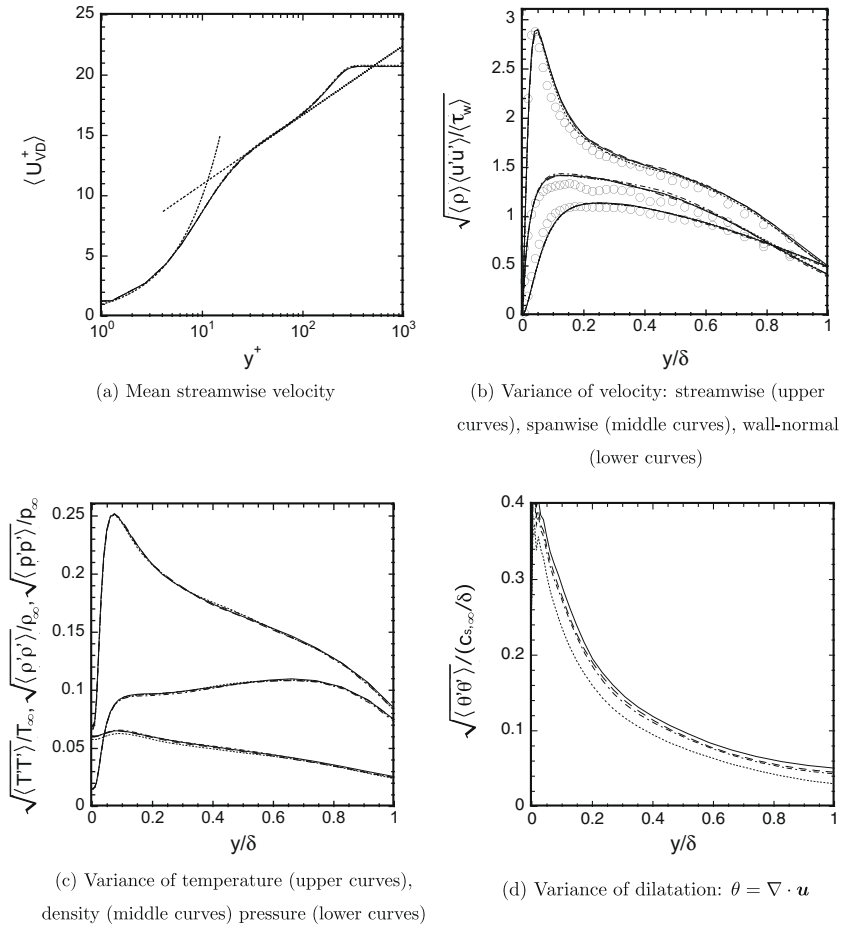
(a) Mean streamwise velocity

(b) Variance of velocity: streamwise (upper curves), spanwise (middle curves), wall-normal (lower curves)

(c) Variance of temperature (upper curves), density (middle curves) pressure (lower curves)

(d) Variance of dilatation: $\theta = \nabla \cdot \boldsymbol{u}$

Fig. 16. Comparison of performance of different artificial bulk viscosity models on supersonic turbulent boundary layer. Solid line, LAD-D2-0; dashed line, LAD-D1-0; dashed-dotted line, LAD-D0-0; dotted line, LAD-S-0; thin dotted lines in (a), $U_{VD}^+ = y^+$ and $U_{VD}^+ = 2.5 \log(y^+) + 5.2$; circle in (b), DNS by Pirozzoli et al. [35].

to the dilatation based models. We note that the insensitivity of the predicted statistics to the bulk viscosity models is possibly due to the Van Driest wall-damping function employed in the models (LAD-D1-0, LAD-D0-0 and LAD-S-0) that damps the bulk viscosity near the wall. However, the models without the wall-damping function encounter the numerical instability at the maximum inviscid CFL number of 0.88 using both the explicit and implicit time-integration methods and suffer from extremely severe time-step restriction due to the viscous CFL condition induced by unnecessarily high artificial bulk viscosity near the wall. We also note that due to the Ducros switching, the LAD-D2-0 does not require the wall-damping function for the artificial bulk viscosity.

Fig. 17 shows the mean artificial bulk viscosity distributions. The Van Driest wall-damping exponentially reduces the bulk viscosity toward the wall as shown in the LAD-S-0, LAD-D0-0 and LAD-D1-0. The range of the bulk viscosity obtained by the LAD-D2-0 (no wall-damping function) is 0–0.3 within the boundary layer (these low values cannot be seen from the figure), which indicates that there are no strong shocks within the boundary layer. It is clear that the excessive bulk viscosity introduced by the LAD-S-0 damps the dilatational motions. Also it is possible that the excessive bulk viscosity affect the variances of the pressure throughout the boundary layer where the LAD-S-0 shows less fluctuation than the others.

3.3.2. Effect of SGS models

The effect of SGS models, artificial shear viscosity model and dynamic Smagorinsky model, is addressed by fixing the artificial bulk viscosity model as the LAD-D2 and comparing the SGS models. Fig. 18 shows the mean and fluctuating velocity profiles obtained by the LAD-D2-0, LAD-D2–ASV and LAD-D2–DSM. Although the dynamic Smagorinsky model provides a slight improvement in the mean velocity profile compared to the artificial shear viscosity model, the logarithmic region is shifted in both. The LAD-D2-0 is in better agreement with the law of the wall with a logarithmic region. In the fluctuating velocity, the LAD-D2–ASV and LAD-D2–DSM show the higher peak in streamwise velocity fluctuation and less fluctuations in spanwise and wall-normal velocities compared to the LAD-D2-0. The results indicate that the inclusion of a SGS model in
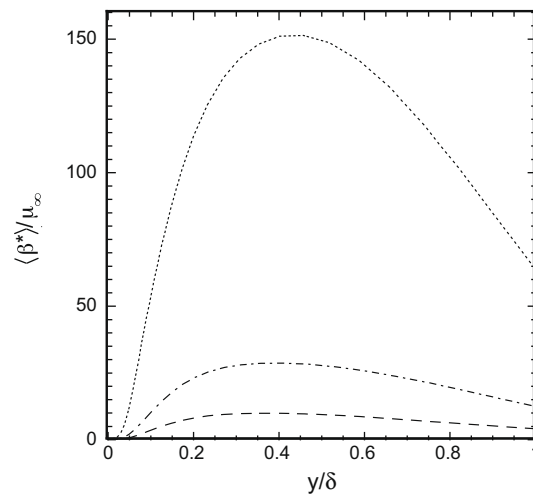
Fig. 17. Mean artificial bulk viscosity distributions within the boundary layer. Solid line, LAD-D2-0; dashed line, LAD-D1-0; dashed-dotted line, LAD-D0-0; dotted line, LAD-S-0.
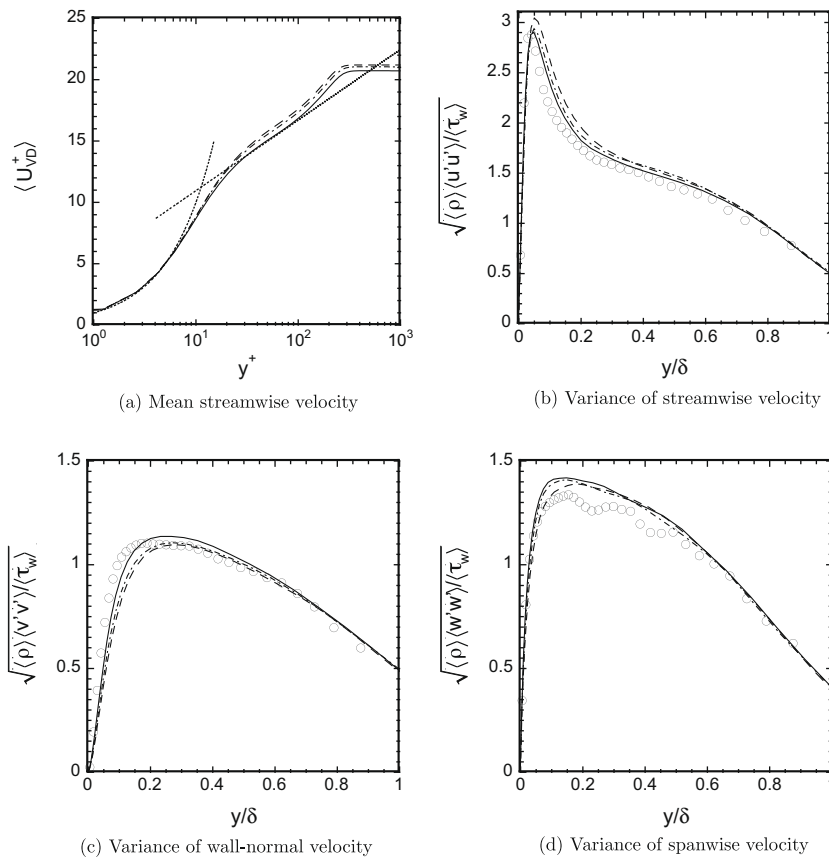

(a) Mean streamwise velocity

(b) Variance of streamwise velocity

(c) Variance of wall-normal velocity

(d) Variance of spanwise velocity

Fig. 18. Comparison of the effect of SGS models on mean and fluctuation velocities in supersonic turbulent boundary layer. Solid line, LAD-D2-0; dashed line, LAD-D2–ASV; dashed-dotted line, LAD-D2–DSM; dotted lines in (a), $U_{VD}^+ = y^+$ and $U_{VD}^+ = 2.5\log(y^+) + 5.2$; circle, DNS by Pirozzoli et al. [35].

addition to the low-pass filtering and artificial bulk viscosity introduces an unnecessary additional numerical dissipation in the resolved turbulence under the relatively moderate Reynolds number examined here. Similar shifts in the mean and fluctuation velocity by adding an explicit SGS model are also observed in the LES of low Mach number ($M_\infty = 0.1$) turbulent channel flow [36] using the very similar numerical schemes but without localized artificial diffusivity.

3.3.3. Effect of implicit time-integration scheme and time-step size

In this section, the accuracy of the implicit time-integration scheme is evaluated by comparing the statistics in the turbulent boundary layer. Simulations are performed by the implicit scheme (Imp2) using the non-dimensional time-step $\Delta t c_{s,\infty}/\delta$ of 0.00125, 0.0025, 0.005 and 0.01. The corresponding time-steps in wall units are $\Delta t^+ = \Delta t u_\tau^2/v = 0.05, 0.1, 0.2$ and 0.4, and the maximum inviscid CFL numbers are 0.44, 0.88, 1.76 and 3.52. The results using the explicit time-integration scheme (RK4) with $\Delta t c_{s,\infty}/\delta = 0.0025$ is also shown for comparisons. The artificial bulk viscosity is fixed to proposed LAD-D2-0 model (no explicit SGS model). Three sub-iterations are carried out within each time-step for the implicit scheme.

Fig. 19 shows the mean and fluctuating velocity profiles obtained by the implicit time-marching methods with varying the time-step size and the explicit method with $\Delta t c_{s,\infty}/\delta = 0.0025$. The predicted mean streamwise velocity and the velocity variances obtained by the implicit time-marching scheme (Imp2) with the three time-step sizes of $\Delta t = 0.00125, 0.0025$ and 0.016 and the explicit scheme (RK4) with $\Delta t = 0.0025$ are in reasonable agreement although the mean velocity profile in a semi-logarithmic plot shows the slight shift by increasing the time-step size in the implicit scheme. Reasonable agreements are also found between the implicit and explicit schemes in terms of the variance of the thermodynamical variables and dilatation (not shown). On the other hand, the results with the large computational time-steps of $\Delta t/\tau = 0.01$ (the time-step in wall units $\Delta t^+ = 0.4$ and maximum CFL number of 3.52) gives different results, including the shift in the mean velocity with a higher value of friction velocity, less fluctuations in streamwise and spanwise velocities and a higher peak in wall-normal velocity fluctuations.

3.4. Sonic jet in a supersonic crossflow

In this section, a more complex illustrative problem of an under-expanded sonic jet injection into a supersonic crossflow is given to show the capability of the proposed bulk viscosity model in a complex application. The flowfield involves 3D unsteady shocks (the front bow shock, upstream separation shock, barrel shock and Mach disk), and jet contact surfaces, with turbulence in both the boundary layer and the jet flow. The second-order implicit time-integration scheme (Imp2) with three sub-iterations is applied to this practical problem. The non-dimensional computational time-step is fixed to 0.0006 at which the maximum inviscid CFL number is less than 1.0.
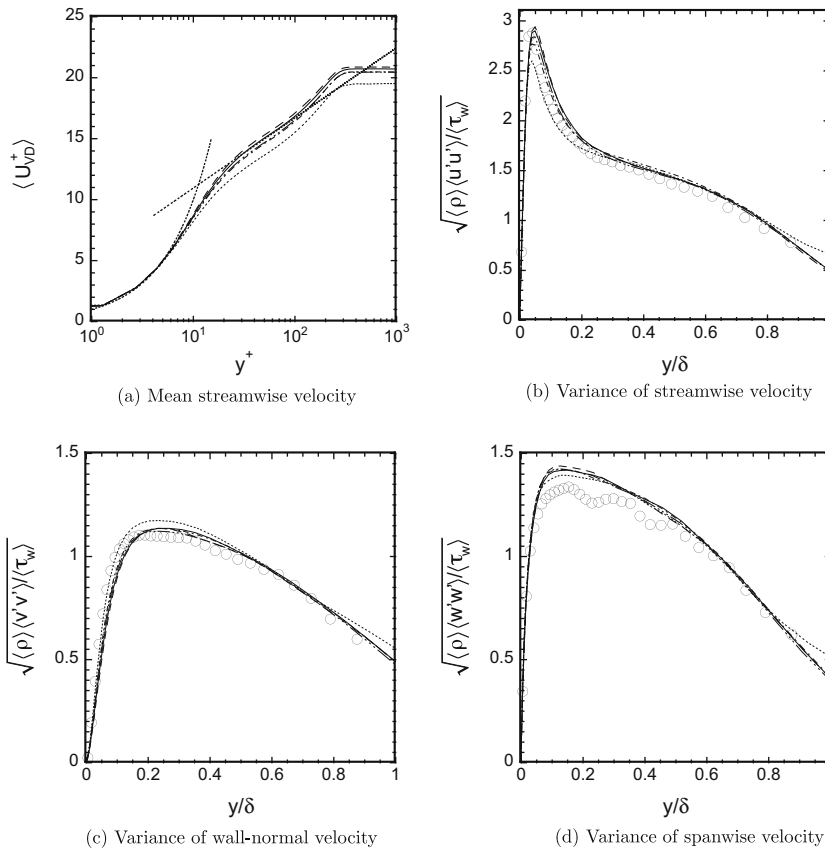

(a) Mean streamwise velocity

(b) Variance of streamwise velocity

(c) Variance of wall-normal velocity

(d) Variance of spanwise velocity

Fig. 19. Comparison of the effect of implicit time-integration scheme and time-step size on mean and fluctuation velocities in supersonic turbulent boundary layer. Solid line, Imp2 $\Delta t = 0.0025$; dashed line, Imp2 $\Delta t = 0.00125$; dashed-dotted line, Imp2 $\Delta t = 0.005$; dotted line, Imp2 $\Delta t = 0.01$; dashed-triple-dotted line, RK4 $\Delta t = 0.0025$; thin dotted lines in (a), $U_{VD}^+ = y^+$ and $U_{VD}^+ = 2.5\log(y^+) + 5.2$; circle, DNS by Pirozzoli et al. [35].

The flow condition examined is based on the experiments of Santiago and Dutton [37]. The computation uses $M_\infty = 1.6$, $Re_D = 2.4 \times 10^4$, where D is the jet nozzle diameter. The density and pressure ratios between the nozzle chamber and crossflow are $\rho_{0j}/\rho_\infty = 5.55$ and $p_{0j}/p_\infty = 8.40$. Based on these flow conditions, the resulting jet-to-crossflow momentum flux ratio is $J = 1.7$. A uniform grid spacing, $\Delta x^+ = \Delta z^+ = 14.5$, is used in streamwise and spanwise directions. In the wall-normal direction, the grid is smoothly stretched from the wall $\Delta y^+_{wall} = 1$ to the uniformly spaced region $\Delta y^+_{unif} = 14.5$. The computational test section where the uniformly spaced mesh is employed extends from the center of the nozzle exit to 5D upstream and downstream in the streamwise direction ($-5 \leqslant x/D \leqslant 5$), 2D on both sides in the spanwise direction ($-2 \leqslant z/D \leqslant 2$) and 3.3D in the wall-normal direction ($0 \leqslant y/D \leqslant 3.3$).

Fig. 20 shows the instantaneous snapshots of the norm of density gradient, the dilatation and the artificial bulk viscosity distributions in the sideview (at midline plane $z/D = 0$). The high-order compact differencing and low-pass filtering schemes with the localized artificial diffusivity methodology captures the 3D unsteady front bow shock, barrel shock, Mach disk and contact surfaces without significant spurious wiggles and also simultaneously resolves the turbulent structures in the downstream mixing region. The strain rate tensor based model (LAD-S) and the dilatation based model (LAD-D0) without switching introduce relatively high artificial bulk viscosity at both the shocks and turbulence regions while the $\mathcal{F}_\beta = S$ based model (LAD-S) gives higher β^* within the turbulence regions. This indicates the need for a shock sensor to localize the bulk viscosity only near shocks. The artificial bulk viscosity with combination of negative dilatation and Ducros-type sensor (Fig. 20(f):
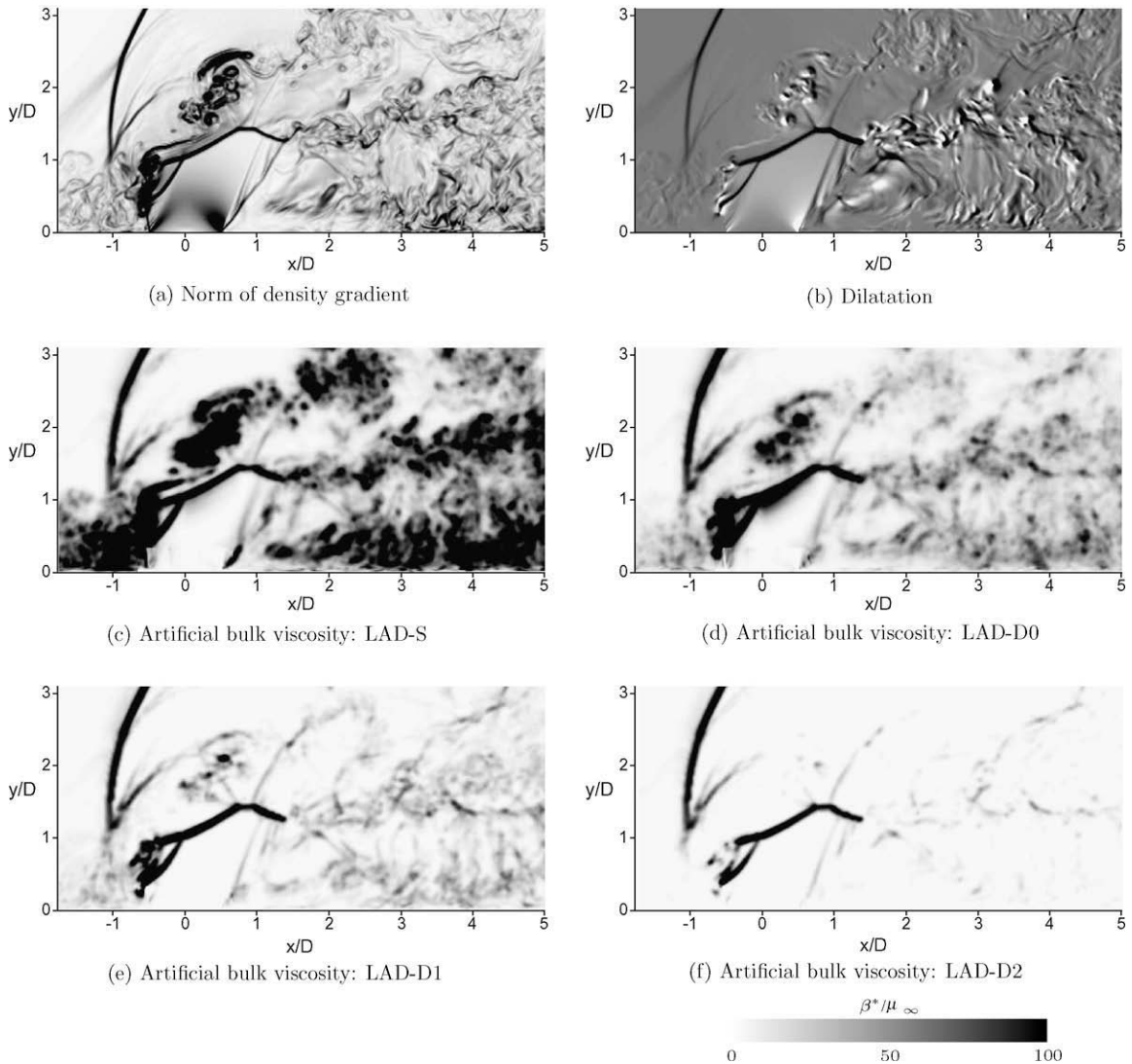

(a) Norm of density gradient

(b) Dilatation

(c) Artificial bulk viscosity: LAD-S

(d) Artificial bulk viscosity: LAD-D0

(e) Artificial bulk viscosity: LAD-D1

(f) Artificial bulk viscosity: LAD-D2

β^*/μ_∞

0   50   100

Fig. 20. Comparison of instantaneous snapshots of the artificial bulk viscosity fields from calculations of sonic jet injection into a supersonic crossflow at midline symmetric plane. Contour levels are from 0 to 7.5 for the norm of density gradient $|\nabla\rho|/(\rho_\infty/D)$, from -10 to 10 for the dilatation $\nabla \cdot \boldsymbol{u}/(c_{s,\infty}/D)$, from 0 to 100 for the artificial bulk viscosity β^*/μ_∞.

LAD-D2 model) is localized at the shocks and automatically vanishes in the regions of weakly compressible turbulence in the boundary layer separation upstream of the jet injection and the downstream jet mixing regions. The LAD-D1 model shows the improvement over the LAD-D0 model but still activates the artificial bulk viscosity at the weak compressible regions. The result illustrates the advantage of the proposed dilatation based bulk viscosity model that is coupled with the negative dilatation and Ducros-type sensor switching. Detailed discussions of the flowfield obtained from these simulations may be found in Ref. [31].

4. Conclusions

We have investigated the performance of the localized artificial diffusivity method for LES of compressible turbulent flows with shocks. The performance of different artificial bulk viscosity models were evaluated through detailed results from the evolution of decaying compressible isotropic turbulence with eddy shocklets and supersonic turbulent boundary layer. Effects of the subgrid-scale models and implicit time-integration scheme/time-step size on compressible turbulent flows were also investigated within the framework of the numerical scheme developed in this paper.

The results illustrate that the artificial bulk viscosity needs a shock sensor to achieve the further improvements. The proposed combination of negative dilatation and Ducros-type switching in dilatation based artificial bulk viscosity showed significant improvements in the capability of the method for simulating the compressible isotropic turbulence with shocks while retaining the shock-capturing capability. The switching function (shock sensor) used in the model effectively removed unnecessary bulk viscosity within expansion and weakly compressible turbulence regions without shocks and allows it to localize near the shocks. Absence of any wall-damping function for the bulk viscosity is another advantage of the proposed model. It should be noted that the flow statistics in the supersonic turbulent boundary layer were relatively less sensitive to the models of the artificial bulk viscosity.

For the moderate Reynolds number, the inclusion of an explicit SGS model results in additional damping of the resolved turbulence. The low-pass filtering and artificial bulk viscosity provide enough numerical damping in the compressible turbulent flows on the LES grids that we have examined in this paper. The compact differencing and filtering schemes coupled with localized artificial diffusivity methodology without adding an explicit SGS model showed better results than with SGS model. Similarly Visbal and Rizzetta [36] and Bogey and Bailly [38,39] also obtained better results without adding an explicit SGS model than with SGS model for the low Mach number isotropic turbulence, channel flow and subsonic jet using high-order central difference and low-pass filtering schemes. Despite these results we caution against the blind practice of implicit (without an explicit SGS model) LES. The relative roles played by the SGS models, low-pass filtering, localized artificial dissipation (added explicitly) and the implicit numerical dissipation depend on the numerical scheme, the grid resolution and quality, Reynolds number, etc. Indeed investigations at the higher Reynolds numbers (highly under-resolved cases) with the present numerical algorithm suggest the need for including a SGS model. We note that the dynamic Smagorinsky model and the artificial shear viscosity model showed very similar results. Also it should be noted that the numerical dissipation introduced by upwind-biased schemes overwhelms a large range of scales although the order of accuracy of the schemes can be very high. Thus, an implicit LES approach with high-order upwind-biased schemes is too dissipative. This is demonstrated by comparing the results for the seventh-order WENO scheme with the proposed artificial bulk viscosity scheme. Our results stress the unintended dissipative effects of upwind-biased numerical scheme, and of the artificial diffusivity and subgrid viscosity. Care in needed in the selection of numerical method and the models used in compressible flow LES and we caution against simple generalizations.

The mean and fluctuation flow quantities obtained by the second-order implicit time-integration scheme with three sub-iterations showed reasonable agreement with the results obtained by the explicit time-marching method if the maximum inviscid CFL number is less than 1.0 for the isotropic turbulence and $1.76(\Delta t^+ = \Delta t u_\tau^2/v = 0.2)$ for the turbulent boundary layer. The localized artificial diffusivity method on highly stretched anisotropic meshes may induce a severe time-step restriction due to the viscous CFL condition as encountered in the jet in a supersonic crossflow computation when using explicit time-marching methods. Considering the time-step restriction the implicit time-integration scheme appeared to be a good compromise approach in terms of accuracy and efficiency especially if the localized artificial diffusivity method on stretched meshes is considered.

Appendix A. One-dimensional shock-related problems

In this appendix 1D inviscid shock-related problems are discussed to investigate the performance of the different artificial bulk viscosity.
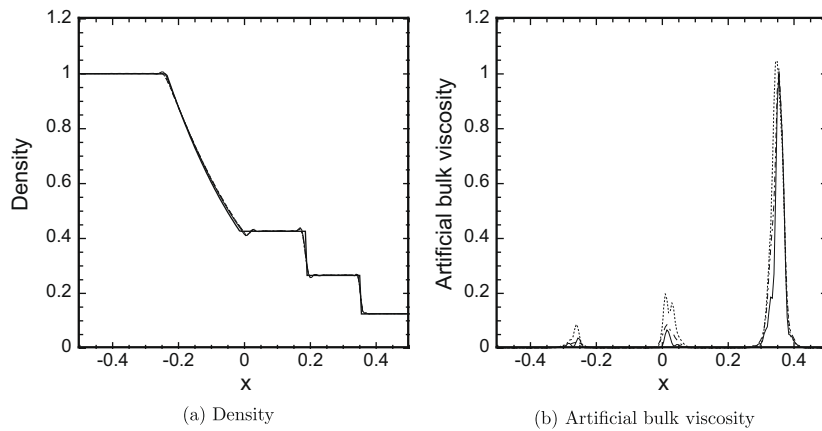

(a) Density

(b) Artificial bulk viscosity

Fig. 21. Numerical simulations of the 1D Sod shock-tube problem. Density and normalized artificial bulk viscosity profiles obtained by LAD-D1-0, LAD-D0-0 and LAD-S-0 are presented at $t = 0.2$. Thin solid line, exact; thick solid line, LAD-D1-0; dashed line, LAD-D0-0; dotted line, LAD-S-0.
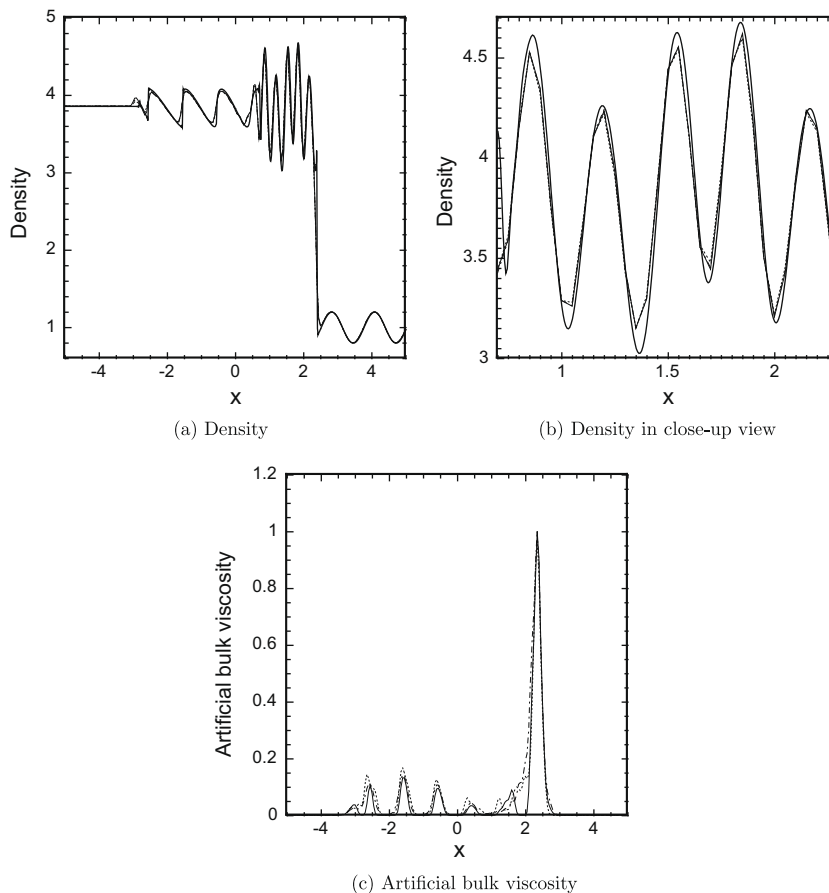

(a) Density

(b) Density in close-up view

(c) Artificial bulk viscosity

Fig. 22. Numerical simulations of the 1D Shu–Osher shock-entropy wave interaction obtained by LAD-D1-0, LAD-D0-0 and LAD-S-0. Density and normalized artificial bulk viscosity profiles are presented at $t = 1.8$. Thin solid line, reference; thick solid line, LAD-D1-0; dashed line, LAD-D0-0; dotted line, LAD-S-0.

A.1. Sod shock-tube problem

The first 1D test case is the shock-tube problem introduced by Sod [12]. The initial left- and right-side conditions are: $\rho_l = 1.0, u_l = 0.0$ and $p_l = 1.0$ for $x \leqslant 0$, and $\rho_r = 0.125, u_r = 0.0$ and $p_r = 0.1$ for $x > 0$. Simulations are performed on a uniformly spaced grid with 201 grid points in the region of $-0.5 \leqslant x \leqslant 0.5 (\Delta x = 0.005)$.

Fig. 21 shows the comparison between the exact solution and the different artificial bulk viscosity models at the time of $t = 0.2$. The artificial bulk viscosity is normalized by the maximum obtained by LAD-D1-0. Note that LAD-D1-0 and LAD-D2-0 reduce to the same scheme for 1D flows. All the models capture the shock and contact discontinuities without significant spurious oscillations and show almost identical results. The negative dilatation switching used in LAD-D1-0 does not show any detrimental effect on capturing the moving discontinuities. The dilatation based artificial bulk viscosity (LAD-D0-0 and LAD-D1-0) gives a smaller amount at the edges of the expansion wave than the strain rate tensor based bulk viscosity (LAD-S-0) while all the models shows a comparable profile at the shock.

A.2. Shu–Osher problem

The second 1D test case is the shock-entropy wave interaction introduced by Shu and Osher [13]. Because the entropy waves are sensitive to the numerical dissipation, excessive numerical dissipation damps the entropy waves. Initial left- and right-side conditions are: $\rho_l = 3.857143, u_l = 2.629369$ and $p_l = 10.33333$ for $x < -4$, and $\rho_r = 1 + 0.2\sin(5x)$, $u_r = 0.0$ and $p_r = 1.0$ for $x \geqslant -4$. Simulations are performed on a uniformly spaced grid with 201 grid points where the computational domain is $-5 \leqslant x \leqslant 5$ with $\Delta x = 0.05$.

Fig. 22 shows the comparison between the reference solution and the numerical simulations for the density and artificial bulk viscosity at the time $t = 1.8$. The reference solution is obtained on 1601 grid points with the LAD-D1-0 method. Similarly to Sod shock-tube problem, all the models show almost identical density distributions. The negative dilatation switching reduces the bulk viscosity at the expansion regions. Note that the LAD method shows superior performance in resolving the entropy waves behind the shock compared to seventh- and ninth-order WENO and weighted compact non-linear schemes as shown in Ref. [2].

References

[1] A.W. Cook, Artificial fluid properties for large-eddy simulation of compressible turbulent mixing, Physics of Fluids 19 (5) (2007) 055103.
[2] S. Kawai, S.K. Lele, Localized artificial diffusivity scheme for discontinuity capturing on curvilinear meshes, Journal of Computational Physics 227 (22) (2008) 9498–9526.
[3] A.W. Cook, W.H. Cabot, A high-wavenumber viscosity for high-resolution numerical method, Journal of Computational Physics 195 (2) (2004) 594–601.
[4] A.W. Cook, W.H. Cabot, Hyperviscosity for shock–turbulence interactions, Journal of Computational Physics 203 (2) (2005) 379–385.
[5] B. Fiorina, S.K. Lele, An artificial nonlinear diffusivity method for supersonic reacting flows with shocks, Journal of Computational Physics 222 (1) (2007) 246–264.
[6] E. Johnsen, J. Larsson, A.V. Bhagatwala, W.H. Cabot, P. Moin, P.S. Rawat, S.K. Shankar, B. Sjogreen, H.C. Yee, X. Zhong, S.K. Lele, Assessment of high-resolution methods for numerical simulations of compressible turbulence with shock waves, Journal of Computational Physics, doi:10.1016/j.jcp.2009.10.028.
[7] A. Bhagatwala, S.K. Lele, A modified artificial viscosity approach for compressible turbulence simulations, Journal of Computational Physics 228 (14) (2009) 4965–4969.
[8] A. Mani, J. Larsson, P. Moin, Suitability of artificial bulk viscosity for large-eddy simulation of turbulent flows with shocks, Journal of Computational Physics 228 (19) (2009) 7368–7374.
[9] P. Moin, K. Squires, W. Cabot, S. Lee, A dynamic subgrid-scale model for compressible turbulence and scalar transport, Physics of Fluids A 3 (11) (1991) 2746–2757.
[10] D.K. Lilly, A proposed modification of the Germano subgrid-scale closure method, Physics of Fluids A 4 (3) (1992) 633–635.
[11] S. Lee, S.K. Lele, P. Moin, Eddy shocklets in decaying compressible turbulence, Physics of Fluids A 3 (4) (1991) 657–664.
[12] G.A. Sod, A survey of several finite difference methods for systems on non-linear hyperbolic conservation laws, Journal of Computational Physics 27 (1) (1978) 1–31.
[13] C.W. Shu, S.J. Osher, Efficient implementation of essentially nonoscillatory shock capturing schemes II, Journal of Computational Physics 83 (1) (1989) 32–78.
[14] S.K. Lele, Compact finite difference schemes with spectral-like resolution, Journal of Computational Physics 103 (1) (1992) 16–42.
[15] D.V. Gaitonde, M.R. Visbal, High-order schemes for Navier–Stokes equations: Algorithm and implementation into FDL3DI, AFRL-VA-WP-TR-1998-3060, Air Force Research Laboratory, 1998.
[16] D.V. Gaitonde, M.R. Visbal, Padé-type higher-order boundary filters for the Navier–Stokes equations, AIAA Journal 38 (11) (2000) 2103–2112.
[17] D.V. Gaitonde, J.S. Shang, J.L. Young, Practical aspects of high-order accurate finite-volume schemes for electromagnetics, AIAA Paper 97–0363, AIAA, 1997.
[18] D.J. Fyfe, Economical evaluation of Runge–Kutta formulae, Mathematics of Computation 20 (1966) 392–398.
[19] S. Obayashi, K. Fujii, S. Gavali, Navier–Stokes simulation of wind-tunnel flow using LU-ADI factorization algorithm, NASA-TM-100042, NASA, 1988.
[20] N. Iizuka, Study of Mach number effect on the dynamic stability of a blunt re-entry capsule, Ph.D. Thesis, University of Tokyo, 2006.
[21] R.M. Beam, R.F. Warming, An implicit factored scheme for the compressible Navier–Stokes equations, AIAA Journal 16 (1978) 393–402.
[22] S. Yoon, A. Jameson, Lower-upper symmetric-Gauss–Seidel method for the Euler and Navier–Stokes equations, AIAA Journal 26 (9) (1988) 1025–1026.
[23] F. Ducros, V. Ferrand, F. Nicoud, C. Weber, D. Darracq, C. Gacherieu, T. Poinsot, Large-eddy simulation of the shock/turbulence interaction, Journal of Computational Physics 152 (2) (1999) 517–549.
[24] J. Larsson, S.K. Lele, P. Moin, Effect of numerical dissipation on the predicted spectra for compressible turbulence, in: Annual Research Briefs 2007, Center for Turbulence Research, NASA Ames and Stanford University, 2007, pp. 47–57. <http://www.stanford.edu/group/ctr/ResBriefs/ARB07.html>.
[25] G.S. Jiang, C.W. Shu, Efficient implementation of weighted ENO scheme, Journal of Computational Physics 126 (1) (1996) 202–228.
[26] E. Garnier, P. Sagaut, M. Deville, A class of explicit ENO filters with application to unsteady flows, Journal of Computational Physics 170 (1) (2001) 184–204.
[27] J. Larsson, Direct numerical simulation of canonical shock/turbulence interaction, in: Annual Research Briefs 2008, Center for Turbulence Research, NASA Ames and Stanford University, 2008, pp. 101–114. <http://www.stanford.edu/group/ctr/ResBriefs/ARB08.html>.

[28] E. Garnier, P. Sagaut, M. Deville, Large eddy simulation of shock/boundary-layer interaction, AIAA Journal 40 (10) (2002) 1935–1944.
[29] S. Teramoto, Large-eddy simulation of transitional boundary layer with impinging shock wave, AIAA Journal 43 (11) (2005) 2354–2363.
[30] S.C. Lo, G.A. Blaisdell, A.S. Lyrintzis, High-order shock capturing schemes for turbulence calculations, AIAA Paper 2007-827, AIAA, 2007.
[31] S. Kawai, S.K. Lele, Large-eddy simulation of jet mixing in a supersonic turbulent crossflow, AIAA Paper 2009-3795, AIAA, 2009.
[32] G. Urbin, D. Knight, Large-eddy simulation of a supersonic boundary layer using an unstructured grid, AIAA Journal 39 (7) (2001) 1288–1295.
[33] B. Choi, P. Moin, Effects of the computational time step on numerical solutions of turbulent flow, Journal of Computational Physics 113 (1) (1994) 1–4.
[34] E.R. Van Driest, Turbulent boundary layer in compressible fluids, Journal of The Aeronautical Sciences 18 (3) (1951) 145–160.
[35] S. Pirozzoli, M. Bernardini, F. Grasso, Characterization of coherent vortical structures in a supersonic turbulent boundary layer, Journal of Fluid Mechanics 613 (2008) 205–231.
[36] M.R. Visbal, D.P. Rizzetta, Large-eddy simulation on curvilinear grids using compact differencing and filtering schemes, Journal of Fluids Engineering 124 (4) (2002) 836–847.
[37] J.G. Santiago, J.C. Dutton, Velocity measurements of a jet injected into a supersonic crossflow, Journal of Propulsion and Power 13 (2) (1997) 264–273.
[38] C. Bogey, C. Bailly, Decrease of the effective Reynolds number with eddy-viscosity subgrid modeling, AIAA Journal 43 (2) (2005) 437–439.
[39] C. Bogey, C. Bailly, Large eddy simulations of round free jets using explicit filtering with/without dynamic Smagorinsky model, International Journal of Heat and Fluid Flow 27 (4) (2006) 603–610.